MOX-Report No. 28/2021

Design of cellular materials for multiscale topology optimization: application to patient-specific orthopedic devices

Ferro, N.; Perotto, S.; Bianchi, D.; Ferrante, R.; Mannisi, M.

MOX, Dipartimento di Matematica
Politecnico di Milano, Via Bonardi 9 - 20133 Milano (Italy)

mox-dmat@polimi.it http://mox.polimi.it

Design of cellular materials for multiscale topology optimization: application to patient-specific orthopedic devices

Nicola Ferro[1], Simona Perotto[1], Daniele Bianchi[2,4], Raffaele Ferrante[3,4], Marco Mannisi[4]

May 18, 2021

[1] MOX - Dipartimento di Matematica, Politecnico di Milano
Piazza L. da Vinci, 32, I-20133, Milano
{nicola.ferro, simona.perotto}@polimi.it

[2] Dipartimento di Ingegneria Civile e Architettura, Università degli Studi di Pavia
via Adolfo Ferrata, 5, I-27100, Pavia
daniele.bianchi@unipv.it

[3] Dipartimento di Ingegneria Civile ed Ingegneria Informatica, Università Tor Vergata
via Politecnico, 1, I-00133, Roma
raffaele.ferrante@uniroma2.it

[4] Medere S.r.l.
via Monasterace, 43, I-00118, Roma
{daniele.bianchi, raffaele.ferrante, marco.mannisi}@medere.it

Abstract

A flexible multiscale topology optimization methodology is introduced in order to associate different areas of the design domain with diverse microstructures extracted from a dictionary of optimized unit cells. The generation of the dictionary is carried out by exploiting microSIMPATY algorithm, which promotes the design of free-form layouts. The proposed methodology is particularized to the design of orthotic devices for the treatment of foot diseases. Different patient-specific settings drive the prototyping of customized insoles, which are numerically verified and successively validated in terms of mechanical performances and manufacturability.

Keywords: Multiscale topology optimization, Material design, 3D printing, Orthopedic devices, SIMPATY algorithm, Anisotropic mesh adaptation

1 Introduction

Cellular materials, characterized by a porous microstructure which properly alternates solid and void, have been engineered in the last years to artificially reproduce the lightweight and the strength properties exhibited by some biological systems, such as bones, honeycombs, sponges, and wood. In parallel, the rise of innovative manufacturing techniques, such as additive processes (e.g., 3D printing), promoted the production of cellular materials in very diverse fields of application, for instance, in healthcare, aerospace, defense, construction, and automotive [19, 53, 106].

The strong interest in cellular materials has favoured the proposal of a wide range of analytical, numerical, and experimental methods for an efficient design of new porous materials. In this context, topology optimization represents the reference mathematical methodology. Actually, this technique has been extensively adopted not only to create optimized structures [5, 6, 13, 14, 17, 60, 65, 73, 80, 84, 86, 89, 105], but also to address the design of unit cells optimized with respect to a specific goal [21, 51, 88, 101]. Starting from the seminal work by O. Sigmund [88], inverse and direct homogenization techniques have been massively employed to engineer and validate periodic microstructures [7, 8, 47].

However, it is well known that the topology optimization carried out at a monoscale (either at a macroscale or at a microscale level) may limit structural performances. Multiscale topology optimization has been proposed as a remedy to overcome such limitations [24, 83]. This strategy consists in identifying the optimal alternation of void, solid, and microstructures inside the design domain [9, 10, 42, 45, 102]. The distribution of void, solid, and microstructures can be carried out by the user through a trial-and-error approach, or automatically driven by a topology optimization tool, to match design or performance requirements at the macroscale. Moreover, the same microstructure or a multiplicity of different cells can be used to handle the transition areas between solid and void. The first option confers the same effective properties on the whole design domain, while the coexistence of several topologies at the microscale allows us to locally diversify the property of the macro domain. Finally, the layout of the employed microstructures can be selected a priori, starting from consolidated dictionaries of unit cells [7, 75, 97], or designed from scratch to match the requirement of interest via homogenization techniques [24, 26, 36, 77, 82].

The scenario which provides us the highest flexibility in terms of design of structures with diversified mechanical performances is the one where the microstructures are ad-hoc designed and change across the optimized macro domain. This option clearly represents the most challenging choice in terms of modeling (dedicated optimizations are employed both at the macro- and at the microscale and, possibly, follow different goal quantities, see, e.g., [41]), computational effort (especially, if the optimizations at the macro- and at the microscale are concurrent, see, e.g., [24]) and manufacture (due to intrinsic limits in manufacturability, for

instance, associated with the transition among different cells, or to possible defects or irregularities characterizing the optimized layouts, see, e.g., [30]).

In this paper, we propose a highly flexible procedure for multiscale topology optimization characterized by a computationally affordable burden, based on a recent and already successfully validated structural design methodology, which provides some improvements in terms of manufacturability. This procedure consists of two phases. During the first one, we create a dictionary of unit cells characterized by the same or by a different topology, sharing the same mechanical objective. In the second phase, we exploit the multiscale topology optimization strategy proposed in [102], combined with a suitable density material thresholding, to identify the areas of the macro domain to be associated with the different microstructures.
The computational complexity of the proposed procedure remains limited thanks to a sequential optimization of the unit cells and of the macrostructure. The independence between the macro- and the microscale allows us to increase the flexibility of the modeling, since different goal quantities can be adopted to drive the optimization of the cells and of the macro layout. Moreover, the generation of the dictionary relies on the recent algorithm microSIMPATY [36], which combines homogenization techniques together with the SIMP method and a customized selection of the computational mesh, generalizing the SIMPATY algorithm proposed in [72] to a microscale. The blending of these three ingredients results in a cost-effective procedure, which provides very smooth layouts, thus limiting the post-processing before manufacturing. It has also been checked that microSIMPATY promotes the design of new topologies in accordance with a free-form paradigm [26, 36]. The computational and practical advantages characterizing the methodology supporting SIMPATY and microSIMPATY algorithms have been already successfully verified in several contexts, involving also shape optimization [37], model reduction [34] and new metamaterial design [26, 36].

MicroSIMPATY algorithm is employed in this paper for the first time into a multiscale topology optimization setting to tackle a biomedical case study as a new application context. Indeed, we focus on the design of an optimized patient-specific insole for the treatment of foot problems [59, 68]. Many conditions are associated with foot diseases, such as musculoskeletal disorders, foot deformity, foot ulceration [52]. The impairments led by foot problems include a higher risk of falling, lower ability to execute standard activities of daily living, and a general lower level of quality of life [46, 63]. Among the different interventions and pain management strategies, foot orthotics represent a very common conservative solution, although an open debate on the correlated effectiveness and biomechanical contribution is still ongoing [66]. Despite that, the reduction of plantar pressure remains a reference target to improve patient's condition [96], typically ensuring the attenuation of symptoms for different pathologies [22, 25]. For this reason, several methods have been proposed to optimize the design and the production of patient-specific foot orthotics, guaranteeing a therapeutic effect [1, 94]. The methodology proposed in this paper is meant to provide a contribution in such a context, relying on

the flexibility and on the good design and manufacturing properties characterizing microSIMPATY algorithm.

The paper is organized as follows. Section 2 introduces the SIMPATY algorithm after a brief recap on the SIMP method. Section 3 is devoted to the homogenization techniques, with a particular emphasis on the inverse methodology, directly involved in the microstructural design. In Section 4, we exploit inverse homogenization to generate two dictionaries of unit cells, different for the number of included microcellular topologies. The adopted multiscale topology optimization is described in Section 5 and applied to the design of optimized orthotic devices in Section 6. Here, two different patient-specific configurations are analyzed for the prototyping of customized insoles. The two scenarios are numerically verified and the most meaningful setting from a medical viewpoint is successively validated in terms of mechanical properties and 3D printing manufacturability. Finally, in the last section, some conclusions are drawn and some hints are provided on possible future developments.

2 A generic setting for structural topology optimization

Topology optimization aims at allocating the material inside the design domain in order to match a goal quantity strictly related to the application at hand, while satisfying specific physical and design constraints.
Originally, topology optimization has been settled to deal with structural problems (see, e.g., the landmark papers by A.G.M. Michell [73], G.I.N. Rozvany [84, 85, 86], M.P. Bendsøe and N. Kikuchi [13]). In this context, the stiffness, the stress, the vibration modes and the mass of the structure are classical examples of target quantities or constraints to the optimization, in combination with the state equation which models the physical law the structure is subject to.
Successively, the crucial impact of topology optimization has been verified in several engineering fields different from structural mechanics (see, e.g., [3, 18, 27, 43, 54, 80, 98, 104] and the references therein). The employment of topology optimization in a wide range of different settings motivated the proposal in the literature of several mathematical and numerical methodologies. Among the most popular approaches, we mention density-based schemes [14, 89], level-set methods [6, 65], topological derivative procedures [91], phase field techniques [17, 28], evolutionary approaches [105], homogenization [5, 13], performance-based optimization [60], and more recently, model reduction and machine learning tools [4, 23, 34, 87, 103]. The main feature distinguishing these methodologies is the modeling expedient adopted to track the solid/void alternation in the design domain, with pros and cons for each possible choice. In this paper, we opt for a density-based scheme, i.e., the Solid Isotropic Material with Penalization (SIMP) method. For an insight review on SIMP we refer to [85].

2.1 The SIMP method

SIMP has been employed for several applications to drive topology optimization, including fluid dynamics [16], acoustics [108], heat transfer [79], electromagnetism [57], electro-mechanics [74], electro-thermo-mechanics [67], fatigue and static failure [55], medicine [92], optics [109], automotive design and manufacturing [38], and aerospace engineering [110]. These references provide just possible examples of the many papers available in the specialized literature.

SIMP introduces an auxiliary function $\rho \in L^\infty(\Omega,[0,1])$, referred to as density or design variable, which models the distribution of the material in the so-called design domain $\Omega \subset \mathbb{R}^2$, here identified with a two-dimensional setting. Ideally, ρ is assumed to take only the extreme values, 0 and 1, where $\rho = 1$ identifies the material whereas $\rho = 0$ characterizes the void. In practice, ρ takes all the values in $[0,1]$. This leads very often to an over-diffused material-void interface in correspondence with intermediate densities, whose physical interpretation is not straightforward. To overcome this issue, SIMP penalizes the intermediate densities by means of a suitable function of ρ.

The generic formulation of the SIMP method looks for the optimal material distribution inside the design domain according to a selected goal quantity, subject to constraints, which take into account the physical configuration at hand together with design requirements. It reads as

$$\min_{\rho\in L^\infty(\Omega,[0,1])} \mathcal{G}(u(\rho),\rho) \; : \begin{cases} a_\rho(u(\rho),v) = F_\rho(v) \quad \forall v \in \mathcal{U} \\ c_m \le C(u(\rho),\rho) \le c_M \\ \rho_{\min} \le \rho \le \rho_{\max}, \end{cases} \tag{1}$$

where $\mathcal{G}(\cdot,\cdot)$ is the target functional to be optimized, the first constraint coincides with the weak form of the equation modeling the physics, the second one enforces a control on the system, with c_m and c_M the corresponding lower and upper bounds, while the last two-sided inequality guarantees the well-posedness of the weak form, being $0 < \rho_{\min} < \rho_{\max} \le 1$, and where $\mathcal{U}$ denotes a Sobolev space strictly dependent on the boundary data characterizing the physical model [31].
Notice that the weak form includes the density function according to a law, which depends on the phenomenon under investigation. For instance, a suitable power of ρ multiplies the stiffness tensor when optimizing structures in a linear regime [12]; in a fluid-dynamic setting, it is standard to consider a density-weighted inverse permeability [16]; in the design of microstructures, ρ modifies the homogenization applied at the microscale [88].
Moreover, the system can be multi-constrained, so that relation $c_m \le C(u(\rho),\rho) \le c_M$ in (1) is replaced by a set of constraints (see Section 5).
Different algorithms are used in the literature to manage the constrained minimization in (1), such as MMA [93], IPOPT [100], heuristic-based, genetic or machine learning routines [23].

When dealing with a structural topology optimization at the macroscale, it is com-

mon to identify the state equation in (1) with the linear elasticity problem in the small displacement regime, so that the bilinear form becomes

$$a_\rho(\mathbf{u}(\rho),\mathbf{v}) = \int_\Omega \sigma_\rho(\mathbf{u}(\rho)) : \varepsilon(\mathbf{v})\, d\Omega, \tag{2}$$

where $\mathbf{u} : \Omega \to \mathbb{R}^2$ denotes the displacement of the structure; $\varepsilon(\mathbf{v}) = (\nabla\mathbf{v} + \nabla\mathbf{v}^T)/2$ is the strain tensor;

$$\sigma_\rho(\mathbf{u}(\rho)) = \rho^p [2\mu\varepsilon(\mathbf{u}(\rho)) + \lambda \mathrm{tr}(\varepsilon(\mathbf{u}(\rho)))I], \tag{3}$$

is the stress tensor penalized by a power law of the density, ρ^p, with $p \geq \max\{1/(1-\nu), 4/(1+\nu)\}$,

$$\lambda = \frac{E_Y \nu}{(1+\nu)(1-2\nu)}, \quad \mu = \frac{E_Y}{2(1+\nu)},$$

the Lamé coefficients, E_Y and ν the Young's modulus and the Poisson's ratio, $\mathrm{tr}(\cdot)$ the trace operator, and I the identity tensor.

Different boundary conditions may characterize the configuration of the structure. Recurrent choices are

$$\mathbf{u}(\rho) = 0$$

to take into account a clamped portion, Γ_D, of the boundary;

$$\sigma_\rho(\mathbf{u}(\rho))\mathbf{n} = \mathbf{f}$$

to model a portion, Γ_N, of the body boundary $\partial\Omega$ loaded by the traction $\mathbf{f} : \Gamma_N \to \mathbb{R}^2$;

$$\sigma_\rho(\mathbf{u}(\rho))\mathbf{n} = \mathbf{0}$$

for a traction-free portion $\Gamma_F \subset \partial\Omega$. It is understood that $\partial\Omega = \Gamma_D \cup \Gamma_N \cup \Gamma_F$, the boundary portions being assumed as closed sets. The selected boundary data define the space $\mathcal{U}$ and the right-hand side, $F_\rho(\mathbf{v})$, in (1).

Problem (1) combined with the state equation (2) may be characterized by multiple local minima, due to the non-convexity of the functional $\mathcal{G}$, so that the uniqueness of the solution is a priori not guaranteed. This is, for instance, the case of the minimum compliance benchmark problem [12, 90]

We discretize the weak form in (1) by means of continuous finite elements, i.e., we look for the displacement, $\mathbf{u}_h$, and the density, ρ_h, in $\mathcal{U}_h = [V_h^r]^2 \cap \mathcal{U}$ and V_h^s, respectively, with

$$V_h^q = \{v \in C^0(\bar{\Omega}) : v|_K \in \mathbb{P}_q \ \forall K \in \mathcal{T}_h\}$$

the space of the finite elements of degree q, $\mathcal{T}_h = \{K\}$ a conforming triangular tessellation of the domain Ω and $\mathbb{P}_q$ the set of polynomials of global degree q, with the understanding that the functions in V_h^0 are discontinuous and piecewise constant on $\mathcal{T}_h$ [31].

It is well-known that SIMP method suffers from several issues related to the discretization adopted in (1). Among the main drawbacks, we list the dependence of the final layout on the grid $\mathcal{T}_h$, the presence of checkerboard and grayscale effects [12, 90], jagged boundaries or too complex topologies which make the optimized design unpractical for manufacturing.
The mesh dependence can be ascribed to the non-uniqueness of the solution. It is generally tackled by constraining or filtering the design variable.
Checkerboard effects arise when solid and void elements alternate in an uneven way. This feature is rather standard in the presence of a two-field formulation, unless an ad hoc combination of the finite element spaces for the displacement, $\mathbf{u}_h$, and the density, ρ_h, is adopted (standard choices are, for instance, $s = 0$, $r = 2$ for quadrilateral elements [14] and $s = 0$, $r = 1$ for triangular elements [20]). Filtering techniques are an alternative viable remedy to get rid of checkerboard patterns, together with adapted computational meshes as detailed in the next section.
Filtering and thresholding techniques can be helpful to manage the presence of the grayscales associated with the intermediate values of ρ_h, between 0 and 1.
Jagged material/void interfaces can be traced back to excessively coarse grids, whereas thin struts often depend on the employment of too fine meshes. As a compromise between too coarse and too fine meshes, in [37, 72] the authors propose a new algorithm, presented in the next section, which enriches the SIMP method with a customized choice of the computational mesh in the framework of structural optimization.

2.2 The SIMPATY algorithm

SIMPATY algorithm (SIMP with AnisoTropic mesh adaptivitY) has been proposed in [72] to assist the design of lightweight and stiff structures aimed at aerospace applications. This new algorithm consists of an iterative procedure, which sequentially alternates the topology optimization in (1), tackled by the Interior Point OPTimizer (IPOPT) package [99, 100], with the generation of an anisotropic adapted mesh.

The benefits guaranteed by adapted computational grids are widely recognized by the availability of devoted tools in the majority of commercial software. Actually, by optimizing the element size, standard isotropic adapted meshes allow us to improve the solution accuracy for a certain mesh cardinality or, vice versa, to contain the number of elements for a user-defined tolerance on the numerical approximation. These improvements are further enhanced by anisotropic grids, which tune the size, the shape, and the orientation of the mesh triangles in order to track the directional features of the modeled phenomena, such as steep boundary and internal layers, discontinuities, sharp fronts, shocks in compressible flows, more in general areas where the problem exhibits strong gradients [11, 29, 33, 39, 40, 64, 71, 81]. The generation of anisotropic grids deserves more technicalities when compared with an isotropic context. This justifies the limited availability of anisotropic mesh

adaptation modules in current simulation software.
Anisotropic mesh adaptation can be driven by heuristic or theoretically sound quantifiers. The first class exploits information prompted by the application at hand in terms of numerical solution or associated variation (e.g., gradient or Hessian). The second class is represented by the a priori and the a posteriori error estimators, which can be classified according to the controlled quantity adjusting the allocation of the elements in the adapted mesh [2].

After discretizing both the displacement and the density with affine finite elements, SIMPATY algorithm resorts to an a posteriori anisotropic recovery-based error estimator, η, associated with the density variable. This estimator turns out to be the ideal tool to identify the steep gradients of ρ across the material/void interface, since it controls the H^1-seminorm of the discretization error, $e_\rho = \rho - \rho_h$. The idea formalized by a recovery-based error estimator is very straightforward [111]. It consists in replacing in the definition of $|e_\rho|_{H^1(\Omega)}$ the exact gradient of the solution with the so-called recovered gradient so that

$$|e_\rho|^2_{H^1(\Omega)} = \int_\Omega |\nabla\rho - \nabla\rho_h|^2 d\Omega \simeq \eta^2 = \int_\Omega |P(\nabla\rho_h) - \nabla\rho_h|^2 d\Omega, \tag{4}$$

with $P(\nabla\rho_h) \in [V_h^q]^2$ a suitable polynomial reconstruction of the exact gradient $\nabla\rho$, for $q \geq 0$.

Recovery-based error estimators have been exploited in several engineering contexts (see, e.g., [50, 71, 76, 81, 107]). The popularity of these estimators is justified by the good properties they have, among which we cite the independence of the specific problem and of the adopted discretization; the computational cheapness; the handy implementation; the high performance in very diverse fields of application. On the other hand, the theoretical investigation of these estimators remains limited to very regular grids, far from the outcome of a mesh adaptation procedure. Concerning the choice of the recovery operator P in (4), several proposals have been made in the literature, to target specif problem- or theoretical-driven requirements. In general, $P(\nabla\rho_h)$ is expected to provide a better approximation to $\nabla\rho$ with respect to $\nabla\rho_h$. Standard rules identify P with a local projection or average of the discrete gradient. Here, we adopt the area-weighted average of $\nabla\rho_h$ over the patch of elements, $\Delta_K = \{T \in \mathcal{T}_h : T \cap K \neq \emptyset\}$, associated with the generic element $K \in \mathcal{T}_h$, being

$$P(\nabla\rho_h)(\mathbf{x}) = |\Delta_K|^{-1} \sum_{T \in \Delta_K} |T| \, \nabla\rho_h\big|_T \quad \text{for any } \mathbf{x} \in K, \tag{5}$$

$|\omega|$ denoting the measure of the generic domain $\omega \subset \mathbb{R}^2$, so that $P(\nabla\rho_h) \in [V_h^0]^2$. Despite the low polynomial degree, the recovered gradient in (5) proved to be a good approximation for $\nabla\rho$ [32, 35, 36, 37, 70, 71, 72, 81], due to the large number of elements contributing to the average.

In 2010, a generalization of the recovery-based error estimators to an anisotropic setting has been proposed in [70]. This extension exploits the anisotropic setting

proposed in [39]. Here, the generic element K of the mesh $\mathcal{T}_h$ is characterized by the elementwise metric $\mathcal{M}_K = \{\lambda_{i,K}, \mathbf{r}_{i,K}\}_{i=1,2}$, with $\lambda_{1,K} \geq \lambda_{2,K} > 0$. In more detail, the lengths $\lambda_{i,K}$ and the orthonormal vectors $\mathbf{r}_{i,K}$ identify the ellipse, $\mathcal{E}_K$, circumscribed to K, which coincides with the push-forward of the circle circumscribed to the reference triangle $\hat{K}$ via the standard affine map $T_K : \hat{K} \to K$ [31]. In particular, the scalar quantities $\lambda_{i,K}$ measure the lenghts of the semi-axes of $\mathcal{E}_K$, whereas the unit vectors $\mathbf{r}_{i,K}$ provide the corresponding directions. To quantify the deformation of the element K, it is standard to adopt the so-called aspect ratio $s_K = \lambda_{1,K}/\lambda_{2,K} \geq 1$, with $s_K = 1$ for equilateral triangles.

The anisotropic variant of the recovery-based error estimator in [111] relies on the correspondence, up to an area-dependent scaling factor,

$$|v|_{H^1(\Delta_K)} \rightleftharpoons \Big[\sum_{i=1}^{2} \lambda_{i,K}^2 (\mathbf{r}_{i,K}^T G_{\Delta_K}(\nabla v)\mathbf{r}_{i,K})\Big]^{1/2}, \tag{6}$$

between the H^1-seminorm of a function $v \in H^1(\Delta_K)$ and the anisotropic counterpart proposed in [39], where $G_{\Delta_K}(\cdot)$ is the symmetric positive semi-definite matrix with entries

$$[G_{\Delta_K}(\mathbf{z})]_{ij} = \sum_{T \in \Delta_K} \int_T z_i z_j \, dT \quad \text{for} \quad i,j = 1,2, \;\; \mathbf{z} = (z_1, z_2) \in [L^2(\Omega)]^2.$$

In (6), the first order derivatives defining the H^1-seminorm are projected along directions $\mathbf{r}_{i,K}$'s, to comply with the anisotropic characterization of the element K.

A cross-comparison between (4) and (6) leads to the anisotropic error estimator

$$\eta^2 = \sum_{K \in \mathcal{T}_h} \eta_K^2 \quad \text{with} \quad \eta_K = \Big[\frac{1}{\lambda_{1,K}\lambda_{2,K}} \sum_{i=1}^{2} \lambda_{i,K}^2 (\mathbf{r}_{i,K}^T G_{\Delta_K}(\mathbf{e}_\rho^\nabla)\mathbf{r}_{i,K})\Big]^{1/2}, \tag{7}$$

where $\mathbf{e}_\rho^\nabla = P(\nabla\rho_h) - \nabla\rho_h$ denotes the recovered error associated with the material density.

Following [69], estimator η is exploited to generate an anisotropic adapted mesh. This goal is pursued by resorting to an iterative procedure, whose generic $\mathtt{j}$-th iteration consists of the following steps:

i) computation of the density function $\rho_h^{\mathtt{j}}$, solution to problem (1), on the mesh $\mathcal{T}_h^{\mathtt{j}}$;

ii) evaluation of the a posteriori error estimator (7) for $\rho_h = \rho_h^{\mathtt{j}}$;

iii) derivation of the piecewise constant metric $\mathcal{M}^{\mathtt{j}}$ on $\mathcal{T}_h^{\mathtt{j}}$;

iv) projection of the metric $\mathcal{M}^{\mathtt{j}}$ into a piecewise linear metric $\widetilde{\mathcal{M}}^{\mathtt{j}}$ on $\mathcal{T}_h^{\mathtt{j}}$;

v) generation of the adapted mesh $\mathcal{T}_h^{\mathtt{j}+1}$ associated with the metric $\widetilde{\mathcal{M}}^{\mathtt{j}}$.

We comment on steps iii)-v), separately, by neglecting the iteration index j to simplify the notation.

Concerning item iii), we look for the elementwise metric $\mathcal{M} = \{\mathcal{M}_K^*\}_{K\in\mathcal{T}_h}$ with $\mathcal{M}_K^* = \{\lambda_{i,K}^*, \mathbf{r}_{i,K}^*\}_{i=1,2}$, the local metric. For the derivation of $\mathcal{M}$ we enforce a certain accuracy on ρ_h, while minimizing the mesh cardinality and equidistributing the error throughout the mesh. These critera give rise to the constrained minimization problem

$$\min_{s_K,\mathbf{r}_{i,K}} \mathcal{J}_K(s_K, \{\mathbf{r}_{i,K}\}_{i=1,2}) : \begin{cases} \mathbf{r}_{i,K}\cdot\mathbf{r}_{j,K} = \delta_{ij} \\ s_K \geq 1, \end{cases} \tag{8}$$

to be solved on each elements K, with δ_{ij} the Kronecher symbol,

$$\mathcal{J}_K(s_K, \{\mathbf{r}_{i,K}\}_{i=1,2}) = s_K\big(\mathbf{r}_{1,K}^T\hat{G}_{\Delta_K}(\mathbf{e}_\rho^\nabla)\mathbf{r}_{1,K}\big) + s_K^{-1}\big(\mathbf{r}_{2,K}^T\hat{G}_{\Delta_K}(\mathbf{e}_\rho^\nabla)\mathbf{r}_{2,K}\big),$$

and $\hat{G}_{\Delta_K}(\mathbf{e}_\rho^\nabla) = G_{\Delta_K}(\mathbf{e}_\rho^\nabla)/|\Delta_K|$. Quantity $\mathcal{J}_K$ follows from the local estimator in (7), being

$$\eta_K^2 = |\Delta_K|\big[s_K\big(\mathbf{r}_{1,K}^T\hat{G}_{\Delta_K}(\mathbf{e}_\rho^\nabla)\mathbf{r}_{1,K}\big) + s_K^{-1}\big(\mathbf{r}_{2,K}^T\hat{G}_{\Delta_K}(\mathbf{e}_\rho^\nabla)\mathbf{r}_{2,K}\big)\big]. \tag{9}$$

Notice that the area information is now confined into the term $|\Delta_K|$. Due to the error equidistribution,

$$\eta_K^2 = |\Delta_K|\,\mathcal{J}_K(s_K, \{\mathbf{r}_{i,K}\}_{i=1,2}) = \text{constant}. \tag{10}$$

Since minimizing the mesh cardinality is equivalent to maximize the area of the mesh elements, the derivation of $\mathcal{M}$ leads us to solve problem (8). In [69, Proposition 26], the authors supply the explicit solution to this problem, namely

$$s_K^* = \sqrt{\gamma_{1,K}/\gamma_{2,K}}, \quad \mathbf{r}_{1,K}^* = \mathbf{g}_{2,K}, \quad \mathbf{r}_{2,K}^* = \mathbf{g}_{1,K},$$

with $\{\gamma_{i,K}, \mathbf{g}_{i,K}\}_{i=1,2}$ the eigen-pairs associated with matrix $\hat{G}_{\Delta_K}(\mathbf{e}_\rho^\nabla)$, with $\gamma_{1,K} \geq \gamma_{2,K} > 0$ and $\{\mathbf{g}_{i,K}\}_{i=1,2}$ orthonormal vectors. Directions $\mathbf{r}_{i,K}^*$ provide the two directions characterizing metric $\mathcal{M}_K^*$, whereas we have only the ratio of the two lenghts $\lambda_{i,K}^*$. To compute $\lambda_{1,K}^*$ and $\lambda_{2,K}^*$, separately, we explicitly impose the error equidistribution, i.e.,

$$\eta_K^2 = \lambda_{1,K}^*\lambda_{2,K}^*|\Delta_{\hat{K}}|\,\mathcal{J}_K(s_K^*, \{\mathbf{r}_{i,K}^*\}_{i=1,2}) = \text{constant} = \frac{\texttt{TOL}^2}{\#\mathcal{T}_h}, \tag{11}$$

with TOL a user-defined tolerance on the density ρ_h, $\#\mathcal{T}_h$ the mesh cardinality, and where relation $|\Delta_K| = \lambda_{1,K}\lambda_{2,K}|\Delta_{\hat{K}}|$ has been exploited, with $\Delta_{\hat{K}} = T_K^{-1}(\Delta_K)$ the pull-back of the patch Δ_K via map T_K.
Since $\mathcal{J}_K(s_K^*, \{\mathbf{r}_{i,K}^*\}_{i=1,2}) = 2\sqrt{\gamma_{1,K}\gamma_{2,K}}$, after straightforward algebraic manipulations, we have

$$\lambda_{1,K}^* = \gamma_{2,K}^{-1/2}\left(\frac{\texttt{TOL}^2}{2\#\mathcal{T}_h|\Delta_{\hat{K}}|}\right)^{1/2}, \qquad \lambda_{2,K}^* = \gamma_{1,K}^{-1/2}\left(\frac{\texttt{TOL}^2}{2\#\mathcal{T}_h|\Delta_{\hat{K}}|}\right)^{1/2},$$

so that the local metric $\mathcal{M}_K^* = \{\lambda_{i,K}^*, \mathbf{r}_{i,K}^*\}_{i=1,2}$ and the metric $\mathcal{M} = \{\mathcal{M}_K^*\}$ are defined.

As far as item iv) is concerned, we commute the elementwise quantities in $\mathcal{M}$ into information associated with the mesh vertices, as it is required by standard mesh generators. For this purpose, we resort to an area-weighted average across the patch of elements associated with each vertex [32, 71]. This step identifies the new metric $\widetilde{\mathcal{M}}$.

Finally, metric $\widetilde{\mathcal{M}}$ is provided as an input to a metric-based mesh generator (see step v)). For the numerical verification in Section 4, we use the software BAMG (Bidimensional Anisotropic Mesh Generator), which is the default geometric discretization tool linked to the adopted solver, FreeFEM [48].

SIMPATY algorithm proved to have remarkable features. The sharp detection of the density across the material/void interface allows us to limit filtering, thus minimizing the post-processing required by standard design tools. Moreover, the same discrete space can be adopted both for the displacement components and the density, thus limiting the computational effort ascribed to the approximation step. These properties guarantee a very cost-effective design procedure, striking a balance between accuracy and computational demands.

SIMPATY algorithm has been successfully applied in [72] to the design of structures optimized with respect to the static compliance in the presence of a one-sided constraint on the mass, and in [35] with respect to the mass of the final layout with a control on the compliance and/or the stress.
SIMPATY has been enriched by shape optimization in [37] to enhance the lightweight and mechanical properties of the optimized configuration, towards an out-of-the-box, free-form paradigm.
Finally, in [34], the authors propose an innovative way to circumvent the computational burden typical of the SIMP approach. The idea is to resort to a Proper Orthogonal Decomposition on SIMP snapshots to predict a rough structure, which is eventually finalized via SIMPATY, in the spirit of an offline/online paradigm [58].

All the references above refer to a topology optimization performed via SIMPATY at the macroscale. In addition, in two preliminary works, SIMPATY algorithm has been modified to optimize microstructures, for the design of new cellular materials [26, 36]. In such a context, problem (1) deserves an ad-hoc formulation which involves the homogenization theory, as detailed in the next section.

3 Homogenization: direct and inverse techniques

We tackle the design of cellular materials, obtained by the periodic repetition of a unit cell, in order to match a required property at the macroscale. A standard approach is the asymptotic homogenization theory, which is, in general, adopted both in a direct and in an inverse form [8, 88]. The basic idea behind direct homog-

enization is to inherit at the macroscale the effects associated with the microscale. In this case, the microscale is the known contribution, whereas the macroscale has to be identified. Vice versa, when dealing with inverse homogenization, we start from a desired feature at the macroscale and we look for the microscopic layout ensuring the expected macroscopic property in the homogenized scale. Some of the methodologies adopted to perform topology optimization at the macroscale have been employed to design the periodic internal structure of cellular materials (see, for instance, [21, 51, 78, 88, 101] where the SIMP, the bidirectional evolutionary structural optimization (BESO) and the level set method are employed). The high versatility of direct and inverse homogenization justifies the adoption of these techniques for diverse applications (see, e.g., [19, 53, 106]).
In this section, we resort to the asymptotic homogenization theory combined with the SIMP method to design new cellular materials. This leads us to solve an optimization problem which can be formalized as in (1), after a suitable redefinition of the quantities involved.

As a reference physical model, we adopt the linear elasticity framework. In particular, it is convenient to consider the componentwise stress-strain ($\sigma-\varepsilon$) relation in terms of the symmetric stiffness tensor E, given by

$$\sigma(\mathbf{u}) = \begin{bmatrix} \sigma_{11}(\mathbf{u}) \\ \sigma_{22}(\mathbf{u}) \\ \sigma_{12}(\mathbf{u}) \end{bmatrix} = \begin{bmatrix} E_{1111} & E_{1122} & E_{1112} \\ E_{1122} & E_{2222} & E_{2212} \\ E_{1112} & E_{2212} & E_{1212} \end{bmatrix} \begin{bmatrix} \varepsilon_{11}(\mathbf{u}) \\ \varepsilon_{22}(\mathbf{u}) \\ 2\varepsilon_{12}(\mathbf{u}) \end{bmatrix} = E\varepsilon(\mathbf{u}), \quad (12)$$

according to the Voigt notation [49].

Direct homogenization incorporates the contribution at the microscale into the macroscale model by modifying the stiffness tensor E [8]. To this aim, it is standard to employ an asymptotic representation of the displacement field, following the two-step procedure:

i) we compute the microscopic displacement, $\mathbf{u}^{*,ij}$, with $ij \in I = \{11, 22, 12\}$, by solving, in the periodic function space $\mathcal{U}_{\#} = [H^1_{\circlearrowleft}(Y)]^2$, the elliptic equation

$$a^{ij}(\mathbf{u}^{*,ij}, \mathbf{v}) := \frac{1}{|Y|}\int_Y \sigma(\mathbf{u}^{*,ij}) : \varepsilon(\mathbf{v})\, dY = \frac{1}{|Y|}\int_Y \sigma(\mathbf{u}^{0,ij}) : \varepsilon(\mathbf{v})\, dY =: F^{ij}(\mathbf{v}), \quad (13)$$

for any $\mathbf{v} \in \mathcal{U}_{\#}$, with Y the design unit cell, $\mathbf{u}^{0,ij}$ a displacement imposed to Y for $ij \in I$, and with $H^1_{\circlearrowleft}(Y)$ the space of functions in $H^1(Y)$ satisfying periodic boundary conditions on ∂Y. In particular, we assign the displacements $\mathbf{u}^{0,11} = [x, 0]^T$, $\mathbf{u}^{0,22} = [0, y]^T$, $\mathbf{u}^{0,12} = [y, 0]^T$, which correspond to the linearly independent engineering strain fields, $\varepsilon^{0,11} = [1, 0, 0]^T$, $\varepsilon^{0,22} = [0, 1, 0]^T$, and $\varepsilon^{0,12} = [0, 0, 1]^T$, respectively;

ii) the computed fields $\mathbf{u}^{*,ij}$ and the imposed ones $\mathbf{u}^{0,ij}$ define the components

of the homogenized stiffness tensor, E^H, according to the relation

$$E^H_{ijkl}(\mathbf{u}^{*,ij},\mathbf{u}^{*,kl}) = \frac{1}{|Y|}\int_Y \left[\sigma(\mathbf{u}^{0,ij}) - \sigma(\mathbf{u}^{*,ij})\right] : \left[\varepsilon(\mathbf{u}^{0,kl}) - \varepsilon(\mathbf{u}^{*,kl})\right] dY, \tag{14}$$

for $ij,kl \in I$.The stiffness tensor E^H takes into account the effect of the microscale. Thus, when dealing with a homogenized context, the linear elasticity equation in (12) is replaced by the stress-strain relation

$$\sigma^H = \begin{bmatrix} \sigma^H_{11}(\mathbf{u}) \\ \sigma^H_{22}(\mathbf{u}) \\ \sigma^H_{12}(\mathbf{u}) \end{bmatrix} = \begin{bmatrix} E^H_{1111} & E^H_{1122} & E^H_{1112} \\ E^H_{1122} & E^H_{2222} & E^H_{2212} \\ E^H_{1112} & E^H_{2212} & E^H_{1212} \end{bmatrix} \begin{bmatrix} \varepsilon_{11}(\mathbf{u}) \\ \varepsilon_{22}(\mathbf{u}) \\ 2\varepsilon_{12}(\mathbf{u}) \end{bmatrix} = E^H \varepsilon. \tag{15}$$

With reference to an inverse homogenization setting, following [88], we design the optimal unit cell ensuring the desired property at the macroscale by means of the SIMP method properly cast in the homogenization framework. To find the optimal distribution of material ρ_m (where the subscript m stands for microscale) in the unit cell, we solve problem (1) where we identify the design domain with Y, and the bilinear and linear forms with

$$\begin{aligned} a^{ij}_{\rho_m}(\mathbf{u}^{*,ij}(\rho_m),\mathbf{v}) &= \frac{1}{|Y|}\int_Y \rho_m^p \sigma(\mathbf{u}^{*,ij}(\rho_m)) : \varepsilon(\mathbf{v})\, dY, \\ F^{ij}_{\rho_m}(\mathbf{v}) &= \frac{1}{|Y|}\int_Y \rho_m^p \sigma(\mathbf{u}^{0,ij}) : \varepsilon(\mathbf{v})\, dY, \end{aligned} \tag{16}$$

respectively, with $\mathbf{v} \in \mathcal{U}_\#$ and $ij \in I$. The design variable ρ_m is selected in $\mathcal{V}_\# = H^1_{\circlearrowleft}(Y)$ to extend the periodic conditions on $\mathbf{u}^{*,ij}$ to the density function. This assumption simplifies the theoretical and numerical discussion below. Concerning the goal functional in (1), we choose

$$\mathcal{G}_m(\mathbf{u}^*(\rho_m),\rho_m) = \mathcal{G}_{ijkl}(\mathbf{u}^{*,ij},\mathbf{u}^{*,kl};\rho_m) = \frac{1}{2}[E^H_{ijkl,\rho_m} - E^G_{ijkl}]^2, \tag{17}$$

where ij, $kl \in I^G \subseteq I$, with $g = \#I^G$, $\mathbf{u}^*(\rho_m)$ is the vector in $[\mathcal{U}_\#]^g$ of components $\mathbf{u}^{*,mn}$, with $mn \in I^G$, $E^H_{ijkl,\rho_m} = E^H_{ijkl,\rho_m}(\mathbf{u}^{*,ij},\mathbf{u}^{*,kl};\rho_m)$ is the tensor defined by

$$E^H_{ijkl,\rho_m} = \frac{1}{|Y|}\int_Y \rho_m^p \left[\sigma(\mathbf{u}^{0,ij}) - \sigma(\mathbf{u}^{*,ij}(\rho_m))\right] : \left[\varepsilon(\mathbf{u}^{0,kl}) - \varepsilon(\mathbf{u}^{*,kl}(\rho_m))\right] dY, \tag{18}$$

E^G_{ijkl}, for $ij,kl \in I^G$, denotes the goal stiffness tensor component adopted by the user to control a physical quantity of interest. Finally, the first box inequality in (1) is reduced to the one-sided constraint on the structure mass

$$C(\mathbf{u}^*(\rho_m),\rho_m) = \mathcal{M}(\rho_m) = \int_Y \rho_m\, dY \leq \alpha|Y|, \tag{19}$$

with $\alpha \in (0,1]$ the maximum allowed volume fraction.

To summarize, problem (1) turns into the following optimization statement:

$$\min_{\rho_m \in L^\infty(Y,[0,1])} \mathcal{G}_m(\mathbf{u}^*(\rho_m),\rho_m) \; : \begin{cases} a^{ij}_{\rho_m}(\mathbf{u}^{*,ij}(\rho_m),\mathbf{v}) = F^{ij}_{\rho_m}(\mathbf{v}) \quad \forall \mathbf{v} \in \mathcal{U}_\#, \\ \mathcal{M}(\rho_m) \le \alpha |Y| \\ \rho_{\min} \le \rho_m \le 1, \end{cases} \tag{20}$$

with $ij \in I^G$.

Analogously to in Section 2.2, the minimization in (20) is carried out by using IPOPT. Among the input quantities to IPOPT, the gradient, $\nabla_{\rho_m}\mathcal{G}(\rho_m)$, of the goal functional in (17) with respect to the density variable ρ_m requires a more careful computation. To this aim, we exploit an adjoint-based Lagrangian formulation, by introducing the augmented functional

$$\mathcal{L}(\mathbf{u}^*,\boldsymbol{\lambda},\rho_m) = \mathcal{G}_{ijkl}(\mathbf{u}^{*,ij},\mathbf{u}^{*,kl};\rho_m) + \sum_{mn\in I^G} [a^{mn}_{\rho_m}(\mathbf{u}^{*,mn}(\rho_m),\boldsymbol{\lambda}^{mn}) - F^{mn}_{\rho_m}(\boldsymbol{\lambda}^{mn})],$$

for ij, $kl \in I^G$. In particular, $\boldsymbol{\lambda} \in [\mathcal{U}_\#]^g$ is the adjoint variable used to impose the state equations, with components $\boldsymbol{\lambda}^{mn}$.

By differentiating $\mathcal{L}$ with respect to $\mathbf{u}^{*,pq}$, we obtain the so-called dual problems

$$[E^H_{ijkl,\rho_m} - E^G_{ijkl}] \frac{\partial E^H_{ijkl,\rho_m}}{\partial \mathbf{u}^{*,pq}}(\mathbf{w}) + a^{pq}_{\rho_m}(\mathbf{w},\boldsymbol{\lambda}^{pq}) = 0 \quad \forall \mathbf{w} \in \mathcal{U}_\#, \tag{21}$$

with $pq \in I^G$; the derivative of $\mathcal{L}$ with respect to $\boldsymbol{\lambda}^{pq}$ leads to the g state equations in (20); finally, the gradient of the goal functional

$$\begin{aligned} \langle \nabla_{\rho_m}\mathcal{G}_m(\rho_m),\phi\rangle &= [E^H_{ijkl,\rho_m} - E^G_{ijkl}] \frac{\partial E^H_{ijkl,\rho_m}}{\partial \rho_m}(\phi) \\ + \quad \sum_{mn\in I^G} \frac{1}{|Y|} \int_Y p\rho_m^{p-1} [\sigma(\mathbf{u}^{*,mn}) - \sigma(\mathbf{u}^{0,mn})] : \varepsilon(\boldsymbol{\lambda}^{mn})\phi \, dY \quad \forall \phi \in \mathcal{V}_\#, \end{aligned} \tag{22}$$

is obtained by deriving $\mathcal{L}$ with respect to ρ_m. Formulas (21) and (22), together with the state equations in (20), constitute the well-known Karush–Kuhn–Tucker (KKT) conditions [61]. These conditions are discretized by employing linear finite elements for both density and displacement, thanks to the use of SIMPATY algorithm in the design of the new cells, so that $\rho_{m,h} \in V_{\#,h}$ and $\mathbf{u}^{*,ij}_h \in [V_{\#,h}]^2$, with $V_{\#,h} = \mathcal{V}_\# \cap V^1_h$ and with $ij \in I^G$.
The resulting algorithm, named microSIMPATY [26, 36], is listed below.

Algorithm 1 : microSIMPATY

Input: $\texttt{CTOL}, \texttt{TOL}, \texttt{TOPT}, \texttt{kmax}, \rho^0_{m,h}, \rho_{\min}, \mathcal{T}_h^0, E^G_{ijkl}, \alpha$

1: Set: $\texttt{k} = 0$, $\text{errC} = 1 + \texttt{CTOL}$
2: **while** $\text{errC} > \texttt{CTOL}$ & $\texttt{k} < \texttt{kmax}$ **do**
3: $\quad \rho^{\texttt{k}+1}_{m,h} = \texttt{optimize}(\alpha, \rho^{\texttt{k}}_{m,h}, \rho_{\min}, E^G_{ijkl}, \mathcal{G}_m, \nabla_{\rho_m}\mathcal{G}_m, \texttt{TOPT})$;
4: $\quad \mathcal{T}_h^{\texttt{k}+1} = \texttt{adapt}(\mathcal{T}_h^{\texttt{k}}, \rho^{\texttt{k}+1}_{m,h}, \texttt{TOL})$;
5: $\quad \text{errC} = |\#\mathcal{T}_h^{\texttt{k}+1} - \#\mathcal{T}_h^{\texttt{k}}|/\#\mathcal{T}_h^{\texttt{k}}$;
6: $\quad \texttt{k} = \texttt{k} + 1$;
7: **end**
8: $\tau = \rho^{\texttt{k}}_{m,h}$;
9: $\mathbf{E}^H(\tau) = \texttt{homogenize}(\tau)$;

Output: τ, $\mathbf{E}^H(\tau)$

The algorithm switches between an optimization phase (function `optimize` in line 3) and a mesh adaptation step (function `adapt` in line 4), based on the anisotropic adaptive strategy detailed in Section 2.2. In particular, three tolerances, together with a maximum number `kmax` of global (optimization+adaptation) iterations, constrain the optimization. In more detail, `CTOL` controls the stagnation of the number of elements between two consecutive mesh adaptations; `TOPT` sets the accuracy for the minimization problem; `TOL` is the user-defined accuracy characterizing the equidistribution of the error throughout the mesh elements according to (11).
MicroSIMPATY algorithm returns the optimized layout τ identified by the distribution of $\rho_{m,h}$ in Y, together with vector

$$\mathbf{E}^H(\tau) = [E^H_{1111,\tau}, E^H_{2222,\tau}, E^H_{1212,\tau}, E^H_{1122,\tau}, E^H_{1112,\tau}, E^H_{2212,\tau}] \tag{23}$$

which gathers the components of the homogenized stiffness tensor in (18) computed on τ, i.e., $E^H_{ijkl,\tau} = E^H_{ijkl,\rho_{m,h}}(\mathbf{u}^{*,ij}, \mathbf{u}^{*,kl}; \tau)$, with $ij, kl \in I$ (function `homogenize` in line 9).

4 Generation of a cellular dictionaries

In this section, we provide two different strategies to generate a collection of different unit cells. We will refer to this ensemble as to a dictionary, $\mathcal{D} = \{\mathcal{W}_1, \ldots, \mathcal{W}_z\}$, consisting of z different words. The generic word $\mathcal{W}_s = (\tau_s, \alpha_s, \mathbf{E}^H(\tau_s))$, with $s = 1, \ldots, z$, gathers the layout τ_s generated by microSIMPATY algorithm, the corresponding volume fraction, α_s, and the associated homogenized stiffness tensor, $\mathbf{E}^H(\tau_s)$, defined as in (23). Without loss of generality, we consider words characterized by different volume fractions, ordered in an ascendant way, and optimized with respect to the same goal quantity $\mathcal{G}_m$, even though for different values E^G.

In particular, we generate two distinct dictionaries. The words of the first ensemble (referred to as single-cellular dictionary) share the same cell topology; vice versa the second set (referred to as multi-cellular dictionary) consists of words with a different topology. To this aim, we adopt a multi-objective framework, where topology optimization is contemporary driven by several goal quantities. This choice is typical of practical contexts such as the one analyzed in Section 6. A first instance of a multi-objective topology optimization carried out by the microSIMPATY algorithm is provided in [26].
A multi-objective formulation of problem (20) implies a generalization of the definition for the goal functional $\mathcal{G}_m$, here identified by the convex combination of functionals as in (17), i.e.,

$$\mathcal{G}_m(\mathbf{u}^*(\rho_m),\rho_m) = \sum_{t=1}^{\vartheta} \beta_t \, \mathcal{G}_{ij_tkl_t}(\mathbf{u}^{*,ij_t},\mathbf{u}^{*,kl_t};\rho_m) = \sum_{t=1}^{\vartheta} \frac{\beta_t}{2} \, [E^H_{ij_tkl_t,\rho_m} - E^G_{ij_tkl_t}]^2, \quad (24)$$

with ij_t, $kl_t \in I^G$, with weights $\beta_t \geq 0$ for $t = 1,\ldots,\vartheta$, such that $\sum_{t=1}^{\vartheta} \beta_t = 1$. The components of the goal stiffness tensor are collected in the vector $\mathbf{E}^G = [E_{ij_tkl_t}]_{t=1}^{\vartheta}$ in $\mathbb{R}^{\vartheta}$, which replaces the scalar input E^G_{ijkl} to microSIMPATY algorithm.

Algorithm 2 provides a unified scheme for the generation of the two dictionaries (with `SvsM` ='S' for the single-cellular dictionary, `SvsM` ='M' for the multi-cellular one). The details of the two procedures are addressed in the next sections.

4.1 Generation of a single-cellular dictionary

A single-cellular dictionary is characterized by a unique topology. We choose the reference layout, τ^R, yielded by microSIMPATY algorithm for the multi-objective goal functional identified by the reference vector $\mathbf{E}^G = \mathbf{E}^{G,R} \in \mathbb{R}^{\vartheta}$, and for an assigned volume fraction, v_f^R, both selected by the user (lines 3-5). In particular, the words in $\mathcal{D}$ are generated via a suitable post-processing of τ^R, which essentially increases or reduces the thickness of the considered layout, according to the volume fractions in the input vector $\mathbf{v}_f = [\mathbf{v}_f(s)]_{s=1}^{z}$ (function `offset` in line 7). For this purpose, we resort to a parametric design platform, which is based on the Rhino 3D CAD software[1] endowed with the embedded visual programming tool Grasshopper[2].

[1] http://www.rhino3d.com/

[2] http://www.grasshopper3d.com/

Algorithm 2 : dictioSIMPATY

Input: CTOL, TOL, TOPT, kmax, $\rho^0_{m,h}$, $\rho_{\min}$, $\mathcal{T}^0_h$, $\mathbf{v}_f$, SvsM

1: $z = \texttt{length}(\mathbf{v}_f)$;
2: **if** SvsM ==‘S’ **then**
3: read v^R_f;
4: read $\mathbf{E}^{G,R}$;
5: $[\tau^R, \mathbf{E}^H(\tau^R)] =$ microSIMPATY(CTOL, TOL, TOPT, kmax, $\rho^0_{m,h}$, $\rho_{\min}$, $\mathcal{T}^0_h$, $\mathbf{E}^{G,R}$, v^R_f);
6: **for** $s = 1, ..., z$ **do**
7: $\tau_s = \texttt{offset}(\tau^R, \mathbf{v}_f(s))$;
8: $\mathbf{E}^H(\tau_s) = \texttt{homogenize}(\tau_s)$;
9: $\mathcal{W}'_s = (\tau_s, \mathbf{v}_f(s), \mathbf{E}^H(\tau_s))$;
10: $\mathcal{D} = \{\mathcal{D}, \mathcal{W}'_s\}$;
11: **end**
12: **end**
13: **if** SvsM ==‘M’ **then**
14: read $\mathbf{E}^G$;
15: **for** $s = 1, ..., z$ **do**
16: $[\tau_s, \mathbf{E}^H(\tau_s)]$ = microSIMPATY(CTOL, TOL, TOPT, kmax, $\rho^0_{m,h}$, $\rho_{\min}$, $\mathcal{T}^0_h$, $\mathbf{E}^G(s,:)$, $\mathbf{v}_f(s)$);
17: $\mathcal{W}'_s = (\tau_s, \mathbf{v}_f(s), \mathbf{E}^H(\tau_s))$;
18: $\mathcal{D} = \{\mathcal{D}, \mathcal{W}'_s\}$;
19: **end**
20: **end**
21: $\mathcal{D} = \texttt{sort}(\mathcal{D})$;

Output: $\mathcal{D}$

The definition of each word $\mathcal{W}'_s$ is completed by computing the homogenized stiffness tensor $\mathbf{E}_H(\tau_s)$ defined as in (23) (function homogenize in line 8).
Finally, the words are sorted for increasing values of the volume fraction (function sort in line 21) to build up the dictionary $\mathcal{D}_S$, all the entries in $\mathbf{v}_f$ being assumed distinct.

We exemplify this procedure by selecting the multi-objective goal functional

$$\begin{aligned} & \mathcal{G}_m(\mathbf{u}^*(\rho_m),\rho_m) = \frac{1}{2}\mathcal{G}_{1111}(\mathbf{u}^{*,11},\mathbf{u}^{*,11};\rho_m) + \frac{1}{2}\mathcal{G}_{2222}(\mathbf{u}^{*,22},\mathbf{u}^{*,22};\rho_m) \\ = \quad & \frac{1}{4}[E^H_{1111,\rho_m} - E^G_{1111}]^2 + \frac{1}{4}[E^H_{2222,\rho_m} - E^G_{2222}]^2. \end{aligned} \tag{25}$$

The two components of the homogenized stiffness tensor here selected are instrumental with a view to the application in Section 6. Concerning the other input parameters to Algorithm 2, we set

$$\begin{gathered} \texttt{CTOL} = \texttt{1e}-\texttt{04}, \quad \texttt{TOL} = \texttt{1e}-\texttt{03}, \quad \texttt{TOPT} = \texttt{1e}-\texttt{06}, \quad \texttt{kmax} = \texttt{10}, \\ \rho^0_{m,h} = |\sin(2\pi x/5)\sin(2\pi y/5)|, \quad \rho_{\min} = \texttt{1e}-\texttt{04}, \end{gathered} \tag{26}$$

with $\mathbf{v}_f = [0.35, 0.4 : 0.1 : 0.9]$, $\mathcal{T}^0_h$ coinciding with a structured 50×50 mesh of the unit cell $Y = (0,10)^2$ [mm^2], and where the flag `SvsM` is set to '`S`' since interested in a single-cellular dictionary. The values set by the user for the reference volume fraction and for the selected homogenized stiffness tensor components are $v^R_f = 0.5$ and $E^G_{1111} = E^{G,R}_{1111} = 2.50\text{e-}01$, $E^G_{2222} = E^{G,R}_{2222} = 1.25\text{e-}01$, respectively. We remark that the components both of the reference and of the homogenized stiffness tensors are scaled with respect to the corresponding full material configuration (i.e., $\rho_m = 1$ in (18)), after setting $E_Y = 45.00$ [N/mm^2] and $\nu = 0.49$ to characterize the base material. Finally, the penalization exponent in (16) is taken equal to 4.

The reference layout, τ^R, yielded by algorithm `microSIMPATY` is the one in panel (e) of Figure 2, whose homogenized stiffness tensor components, E^H_{1111,τ^R}, E^H_{2222,τ^R}, exactly coincide with the corresponding goal values, $E^{G,R}_{1111}$, $E^{G,R}_{2222}$. Starting from τ^R and the volume fractions in $\mathbf{v}_f$, function `offset` returns the layouts in Figure 1. We remark that the employment of a unique optimized topology modified via offset criteria may lead to layouts that are not so handy to be manufactured. For instance, this is the case of the layouts in panels (a) and (f) which exhibit thin struts and small holes, respectively. Moreover, we have verified that volume fractions less than 0.35 yield unprintable configurations.

Function `homogenize` computes the homogenized stiffness tensor characterizing τ_s's. Table 1 provides the values for the two components E^H_{1111,τ_s} and E^H_{2222,τ_s}, for $s = 1,...,z$, whereas we refer to Figure 5 for the values of the other non-null components.

4.2 Generation of a multi-cellular dictionary

A multi-cellular dictionary gathers words which are associated with different topologies. With reference to Algorithm 2, this means that microSIMPATY algorithm is run a number of times equal to z (line 16), after the user selects a multi-objective goal functional (line 14) and for a certain volume fraction. As a result, we introduce the tensor $\mathbf{E}^G \in \mathbb{R}^{z\times\vartheta}$, whose s-th row, for $s = 1,\ldots,z$, collects the goal

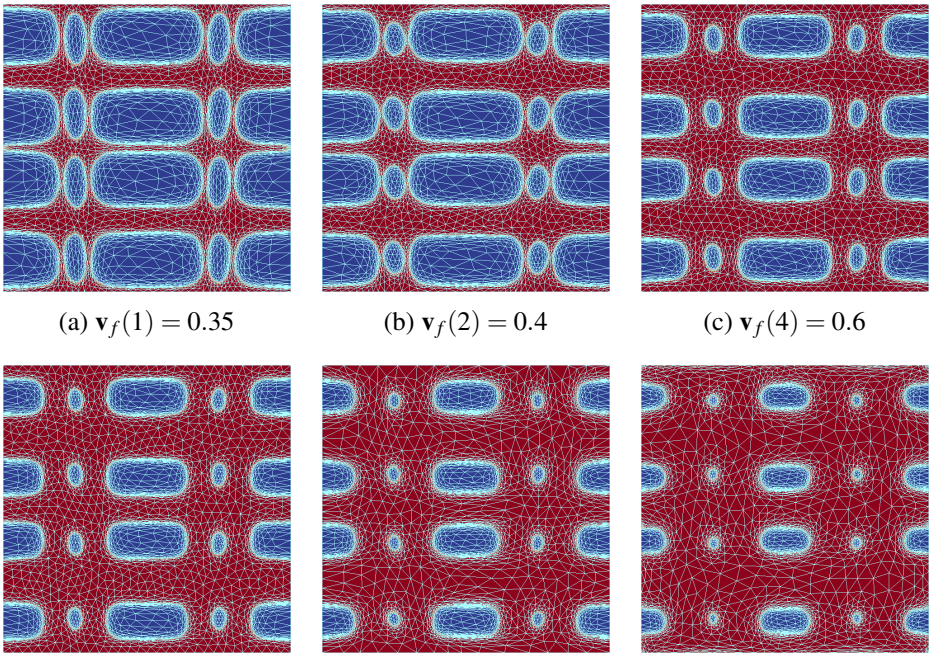

(a) $\mathbf{v}_f(1) = 0.35$ (b) $\mathbf{v}_f(2) = 0.4$ (c) $\mathbf{v}_f(4) = 0.6$

(d) $\mathbf{v}_f(5) = 0.7$ (e) $\mathbf{v}_f(6) = 0.8$ (f) $\mathbf{v}_f(7) = 0.9$

Figure 1: Optimized cells (single-cellular dictionary): density distribution overlapped to the associated anisotropic grid for the different volume fractions in $\mathbf{v}_f$.

values $E^G_{ij_tkl_t}$, with $t = 1,\dots,\vartheta$, defining the functional in (24), whereas vector $\mathbf{v}_f \in \mathbb{R}^z$ gathers the chosen volume fractions. Here, we select $\mathbf{v}_f = [0.1 : 0.1 : 0.9]$, (i.e., $z = 9$), and, for each $s = 1,\dots,9$, we choose the goal functional in (25) (i.e., $\vartheta = 2$), with goal values specified in Table 2, top panel.
As far as the other input parameters to dictioSIMPATY is concerned, we preserve the same values as in (26), while selecting $\mathcal{T}_h^0$ as a structured $N_{\mathcal{T}_h^0} \times N_{\mathcal{T}_h^0}$ mesh of the unit cell $Y = (0,10)^2$ [mm^2], the flag `SvsM` being '`M`' since interested in generating the multi-cellular dictionary, $\mathcal{D}_{\mathtt{M}}$. Notice that, to design the nine layouts, we adopt a initial tessellation of the computational domain characterized by a different value for $N_{\mathcal{T}_h^0}$ (see Table 2, bottom panel). The same base material as well as the same penalization law as in Section 4.1 are here adopted.

s	1	2	3	4	5	6	7
E^H_{1111,τ_s}	1.95e-01	2.23e-01	2.50e-01	3.87e-01	4.77e-01	5.95e-01	7.24e-01
E^H_{2222,τ_s}	6.19e-02	7.85e-02	1.25e-01	2.67e-01	3.65e-01	4.97e-01	6.41e-01

Table 1: Optimized cells (single-cellular dictionary): homogenized values of the goal quantities for the different volume fractions in $\mathbf{v}_f$.

s	1	2	3	4	5	6	7	8	9
E^G_{1111}	1.50e-02	2.75e-02	8.65e-02	1.40e-01	2.50e-01	3.10e-01	3.90e-01	4.30e-01	6.50e-01
E^G_{2222}	1.00e-02	2.27e-02	4.00e-02	6.20e-02	1.25e-01	2.10e-01	2.20e-01	2.65e-01	5.00e-01
$N_{\mathcal{T}_h^0}$	50	40	50	30	50	50	30	50	40

Table 2: Optimized (multi-cellular dictionary): goal values and selected initial mesh for the different volume fractions in $\mathbf{v}_f$.

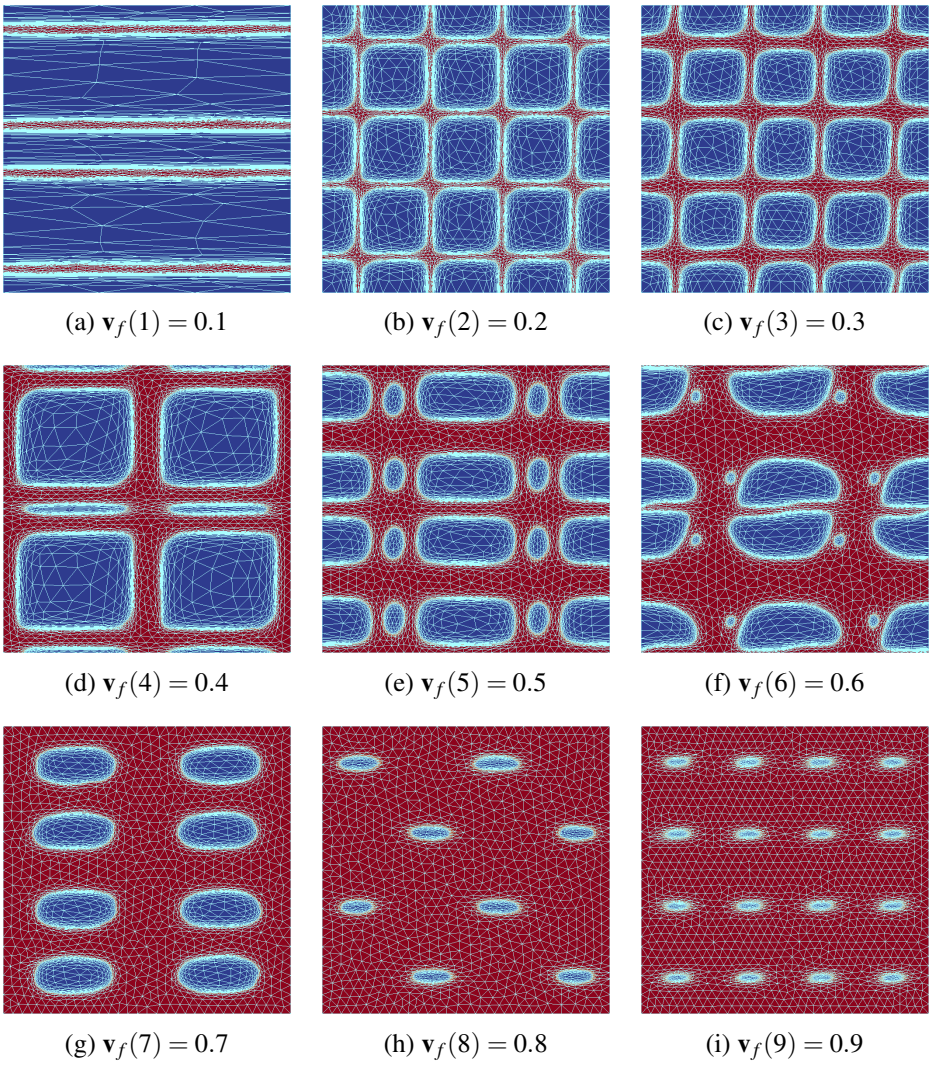

(a) $\mathbf{v}_f(1) = 0.1$ (b) $\mathbf{v}_f(2) = 0.2$ (c) $\mathbf{v}_f(3) = 0.3$

(d) $\mathbf{v}_f(4) = 0.4$ (e) $\mathbf{v}_f(5) = 0.5$ (f) $\mathbf{v}_f(6) = 0.6$

(g) $\mathbf{v}_f(7) = 0.7$ (h) $\mathbf{v}_f(8) = 0.8$ (i) $\mathbf{v}_f(9) = 0.9$

Figure 2: Optimized cells (multi-cellular dictionary): density distribution overlapped to the associated anisotropic grid for the different volume fractions in $\mathbf{v}_f$.

Figure 2 collects the microSIMPATY layouts τ_s, for the diverse volume fractions,

overlapped with the corresponding final anisotropic adapted mesh. The stretched elements of the grids allow to precisely detect the void/material interface, leading to very smooth boundaries, while regularizing the possible sharp angles of the layouts (as a clear example, see the unit cell in panel (d)). Moreover, following [37], to improve the accuracy of the mechanical analysis, we restore an isotropic tessellation in the internal part of the material, so that the stretched elements act only in sharply detecting the topology.
The obtained configurations respond to the different design prescriptions. In more detail, except for the unit cell in panel (a) which is far from being manufacturable, the x-direction turns out to be the preferential one in terms of mass allocation, at least until the volume fraction is sufficiently far from 1. This evidence is fully in agreement with the imposed mechanical requirement which reduces the stiffness in y-direction. More quantitative information about the final adapted mesh, here denoted by $\mathcal{T}_h$ to simplify the notation, is provided in the bottom panel of Table 3 where the cardinality and the maximum aspect ratio of the grid are gathered. We observe that complex topologies require a larger number of elements, whereas the stretching of the mesh elements is strictly related to the size of the holes in the cell layout.

Concerning the homogenized stiffness tensor of the unit cells, we refer to Table 3, top panel, for the components driving the topology optimization and to the markers in Figure 8 for the others. We recognize a good matching between goal and homogenized components.

s	1	2	3	4	5	6	7	8	9
E^H_{1111,τ_s}	1.68e-02	2.93e-02	8.22e-02	1.45e-01	2.50e-01	3.07e-01	3.90e-01	4.78e-01	6.50e-01
E^H_{2222,τ_s}	1.18e-02	2.45e-02	3.98e-02	6.75e-02	1.25e-01	1.98e-01	2.20e-01	3.08e-01	5.00e-01
$\#\mathcal{T}_h$	3664	10912	10796	6704	8030	8552	5862	3436	5080
$s_K^{\max}$	747.00	52.90	37.43	77.21	53.48	74.44	27.34	18.00	13.06

Table 3: Optimized cells (multi-cellular dictionary): homogenized values for the goal quantities; cardinality and maximum aspect ratio for the final adapted mesh for the different volume fractions in $\mathbf{v}_f$.

5 Multiscale topology optimization

In this section, we address the design of a macroscale geometry in terms of optimal allocation of microscopic unit cells. This process, widely employed in practice [9, 10, 42, 45], is generally referred to as multiscale topology optimization.

In accordance with [7, 102], we detail how to employ a dictionary, $\mathcal{D}$, of unit cells, optimized to match a goal quantity G_1 at the homogenized scale, for the design of a structural configuration in order to satisfy a mechanical requirement, G_2, at the

macroscale.
In the literature, both pre-defined [7, 75, 97] and ad-hoc designed [24, 26, 36, 77, 82] cells are employed as words of the dictionary $\mathcal{D}$. We follow the second approach to exploit the dictionaries, $\mathcal{D}_{\mathtt{S}}$ and $\mathcal{D}_{\mathtt{M}}$, generated in the previous section.

The reference framework is still represented by problem (1) which has to be properly customized according to a multiscale formulation. In particular, we have to solve the following problem

$$\min_{\rho_M \in L^\infty(\Omega,[0,1])} \mathcal{G}_M(\mathbf{u}(\rho_M),\rho_M) \; : \begin{cases} a^H_{\rho_M}(\mathbf{u}(\rho_M),\mathbf{v}) = F_{\rho_M}(\mathbf{v}) \quad \forall \mathbf{v} \in \mathcal{U} \\ \mathbf{c}_m \leq \mathbf{C}(\mathbf{u}(\rho_M),\rho_M) \leq \mathbf{c}_M \\ \rho_{\min} \leq \rho_M \leq \rho_{\max}, \end{cases} \tag{27}$$

where $\mathcal{G}_M = G_2$ is the quantity of interest driving the optimization at the macroscale, the bilinear form of the state equation is

$$a^H_{\rho_M}(\mathbf{u}(\rho_M),\mathbf{v}) = \int_\Omega \sigma^H_{\rho_M}(\mathbf{u}(\rho_M)) : \varepsilon(\mathbf{v})\, d\Omega, \tag{28}$$

with $\mathbf{u}(\rho_M) \in \mathcal{U}$,

$$\begin{aligned} \sigma^H_{\rho_M}(\mathbf{u}(\rho_M)) &= \begin{bmatrix} \sigma^H_{11,\rho_M}(\mathbf{u}(\rho_M)) \\ \sigma^H_{22,\rho_M}(\mathbf{u}(\rho_M)) \\ \sigma^H_{12,\rho_M}(\mathbf{u}(\rho_M)) \end{bmatrix} = \Xi^H(\rho_M)\,\varepsilon(\mathbf{u}(\rho_M)) \\ &= \begin{bmatrix} \Xi^H_{1111}(\rho_M) & \Xi^H_{1122}(\rho_M) & \Xi^H_{1112}(\rho_M) \\ \Xi^H_{1122}(\rho_M) & \Xi^H_{2222}(\rho_M) & \Xi^H_{2212}(\rho_M) \\ \Xi^H_{1112}(\rho_M) & \Xi^H_{2212}(\rho_M) & \Xi^H_{1212}(\rho_M) \end{bmatrix} \begin{bmatrix} \varepsilon_{11}(\mathbf{u}(\rho_M)) \\ \varepsilon_{22}(\mathbf{u}(\rho_M)) \\ 2\varepsilon_{12}(\mathbf{u}(\rho_M)) \end{bmatrix}, \end{aligned} \tag{29}$$

and $\Xi^H_{ijkl}(\rho_M)$ the $ijkl$-th component of the multiscale homogenized stiffness tensor, at this level coinciding with a generic function of ρ_M, and F_{ρ_M} takes into account the work due to possible external volume or surface forces. Relation (29) combines, while generalizing, definitions (3) and (15). Indeed, it supports a completely general dependence on the multiscale design variable ρ_M and it contemporary takes into account the effect of the homogenization.

To explicitly define the components of the multiscale homogenized stiffness tensor, Ξ^H, we follow an approach similar to the one adopted in [102].
First of all, we build a possible trend for the six sets of values $\{\alpha_s, E^H_{ijkl,\tau_s}\}_{s=1,\dots,z}$ by means of a polynomial approximation $\Phi^H_{ijkl}(\alpha)$, for $ij, kl \in I$. In particular, the dependence of E^H_{ijkl,τ_s} on α_s is understood due to the implicit relation between the structure volume fraction and layout.
As a next step, we make matrix $\Xi^H(\rho_M)$ computable in Ω to evaluate the bilinear form in (28). For this purpose, for any $\mathbf{x} \in \Omega$, we resort to the identification $\alpha = \rho_M(\mathbf{x})$, and we assign the value $\Phi^H_{ijkl}(\alpha)$ to the component $\Xi^H_{ijkl}(\rho_M(\mathbf{x}))$ (see

Figure 3 for a schematic representation of the implied correspondence between multiscale density and microscopic volume fraction).

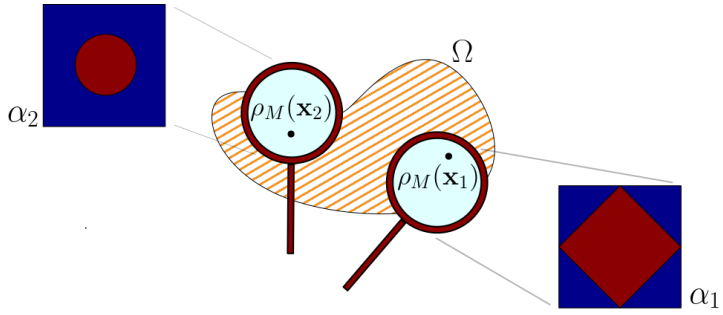

Figure 3: Multiscale topology optimization: correspondence between multiscale density and microscopic volume fraction.

From a computational viewpoint, consistently with the previous sections, we adopt linear finite elements to discretize both the multiscale density and the displacement, i.e., we pick $\rho_{M,h} \in V_h^1$, $\mathbf{u}_h \in [V_h^1]^2 \cap \mathcal{U}$.
The whole multiscale topology optimization is sketched in the algorithm below.

Algorithm 3 : multiscale topology optimization

Input: $\mathcal{D}$, TOPT, $\rho^0_{M,h}$, $\rho_{\min}$, $\rho_{\max}$, $\mathbf{c}_m$, $\mathbf{c}_M$

1: **for** $ij, kl \in I$ **do**
2: $\quad \Phi^H_{ijkl} = \texttt{fitting}(\{\alpha_s, E^H_{ijkl,\tau_s}\}_{s=1,\dots,z})$;
3: $\quad \Xi^H_{ijkl} \leftarrow \Phi^H_{ijkl}$;
4: **end**
5: $\rho_{M,h} = \texttt{optimize}(\mathbf{c}_m, \mathbf{c}_M, \rho^0_{M,h}, \rho_{\min}, \rho_{\max}, \mathcal{G}_M, \nabla_{\rho_M}\mathcal{G}_M, \texttt{TOPT})$;

Output: $\rho_{M,h}$

The algorithm combines, in a sequential way, the fitting of the data at the microscale (in line 2) with the topology optimization at the macroscale (in line 5). The output of the procedure is the discretized multiscale design variable.

6 Design of orthopedic devices

In order to prove the effectiveness of the proposed multiscale topology optimization, we apply the procedure to the design of an orthopedic device. In particular, we focus on the prototyping of new patient-specific insoles for foot treatments, starting from the well-established expertise gained by some of the authors in such an area [66]. The final goal is to manufacture the optimized insole via 3D printing

to check the actual feasibility of the methodology settled in the previous sections.

6.1 Verification

In order to accomplish the design of the patient-specific insole, we resort to Algorithm 3, after introducing some simplifying hypotheses on the physical setting. The main simplification leads us to work on a transverse cut section of the 3D orthopedic device, thus reducing the design domain to a 2D slab in the xy Cartesian plane. Additionally, we assume that the patient-specific configuration is characterized only by three medical conditions for the sole of the foot, i.e., a healthy and an ulcerated zone, together with a possible transition region between these two areas. With a view to the 3D printing of the optimized configuration, the 2D final layout is meant as to be extruded along the z direction.

From a mathematical viewpoint, the optimization of the insole can be cast into the generic framework in (27). In particular, the target functional $\mathcal{G}_M(\mathbf{u}(\rho_M),\rho_M)$ coincides with the mass of the orthotic device

$$\mathcal{G}_M(\mathbf{u}(\rho_M),\rho_M)=\int_\Omega \rho_M d\mathbf{x}.$$

The two-sided constraint in (27) is generalized to different controls to take into account that the stiffness varies according to the local clinical status of the tissue (healthy, ulcerated, or pre-ulcerated). In more detail, the three inequalities

$$\begin{aligned}
\upsilon_m^H &\le \Upsilon^H(\mathbf{u}(\rho_M),\rho_M)\le \upsilon_M^H\\
\upsilon_m^U &\le \Upsilon^U(\mathbf{u}(\rho_M),\rho_M)\le \upsilon_M^U\\
\upsilon_m^T &\le \Upsilon^T(\mathbf{u}(\rho_M),\rho_M)\le \upsilon_M^T,
\end{aligned}$$

are imposed, where

$$\Upsilon^Z(\mathbf{u}(\rho_M),\rho_M)=\frac{1}{\Upsilon_1^Z}\int_{\Gamma^Z}\mathbf{f}\cdot\mathbf{u}(\rho_M)ds$$

denotes the local static compliance computed on the boundary portion $\Gamma^Z\subset\Gamma_N$, with $Z=H$ (healthy tissue), $Z=U$ (ulcerated tissue) and $Z=T$ (transition area between healthy and ulcerated tissue), scaled with respect to the corresponding compliance,

$$\Upsilon_1^Z=\int_{\Gamma^Z}\mathbf{f}\cdot\mathbf{u}(1)ds,$$

in the full-material configuration. Thus, with reference to formulation (27), it follows that

$$\begin{aligned}
\mathbf{c}_m &= [\upsilon_m^H,\upsilon_m^U,\upsilon_m^T]^T,\\
\mathbf{C}(\mathbf{u}(\rho_M),\rho_M) &= [\Upsilon^H(\mathbf{u}(\rho_M),\rho_M),\Upsilon^U(\mathbf{u}(\rho_M),\rho_M),\Upsilon^T(\mathbf{u}(\rho_M),\rho_M)]^T,\\
\mathbf{c}_M &= [\upsilon_M^H,\upsilon_M^U,\upsilon_M^T]^T.
\end{aligned}$$

Finally, the PDE constraining the topology optimization is featured by the bilinear form in (28), the linear form

$$F_{\rho_M}(\mathbf{v}) = \int_{\Gamma_N} \mathbf{f}\cdot\mathbf{v}\, ds,$$

and the function space $\mathcal{U} = H^1_{\Gamma_D}(\Omega)$, where the boundary $\partial\Omega$ of the design domain is subdivided into the portions Γ_D, Γ_N, and $\Gamma_F = \partial\Omega \setminus (\Gamma_D \cup \Gamma_N)$.

We observe that the domain Ω, the load $\mathbf{f}$, and the areas Γ^Z characterize the patient-specific nature of the current modeling. Domain Ω strictly depends on the size of the patient's foot; force $\mathbf{f}$ takes into account the weight and the gait; finally, the configuration of the ulcerated zone identifies the portions Γ^Z, for $Z =$ H, U, T.

Concerning the verification here performed, we select $\Omega = (-150, 150) \times (0, 50)$ [mm^2], $\Gamma_D = \{(x,y) \in \partial\Omega : -150 \le x \le 150, y = 0\}$, $\Gamma_N = \{(x,y) \in \partial\Omega : -150 \le x \le 150, y = 50\}$, and $\mathbf{f}$ as the profile in Figure 4 (left) to model the pressure exerted by the heel, the pad, and the toe on the insole. The values are extracted from experimental data [56].
We analyze two different clinical scenarios, i.e., the case of an abrupt transition between healthy and ulcerated areas (referred to as the H-U setting), and the complete configuration including the three possible status of the tissue (denoted by the H-U-T setting). The two choices essentially differ in the definition of portions Γ^Z, for $Z =$ H, U, T, being

$$\text{H-U}: \begin{cases} \Gamma^U &= \{(x,y) \in \Gamma_N : L_U \le x \le R_U\}, \\ \Gamma^T &= \emptyset, \\ \Gamma^H &= \Gamma_N \setminus \Gamma^U, \end{cases}$$

$$\text{H-U-T}: \begin{cases} \Gamma^U &= \{(x,y) \in \Gamma_N : L_U \le x \le R_U\}, \\ \Gamma^T &= \{(x,y)\Gamma_N : L_T \le x < L_U \ \text{ or } \ R_U < x \le R_T\}, \\ \Gamma^H &= \Gamma_N \setminus (\Gamma^U \cup \Gamma^T), \end{cases}$$

with

$$L_U = -5(20+\sqrt{51}), \quad R_U = -5(20-\sqrt{51}),$$

$$L_T = -\frac{15\sqrt{37}}{2} - 100, \quad R_T = \frac{15\sqrt{37}}{2} - 100$$

(see the panel in Figure 4 (right) for a sketch).

Concerning the adopted discretization, we use linear finite elements to approximate both the design variable, ρ_M, and the displacement, $\mathbf{u}$, on a 150×25 structured computational mesh $\mathcal{T}_h$.

The multiscale optimization of the insole will be now driven by the dictionaries, $\mathcal{D}_{\mathtt{S}}$ and $\mathcal{D}_{\mathtt{M}}$, created in Sections 4.1 and 4.2, respectively. In particular, the functional in (25) constraining the design of the words of the two dictionaries has been

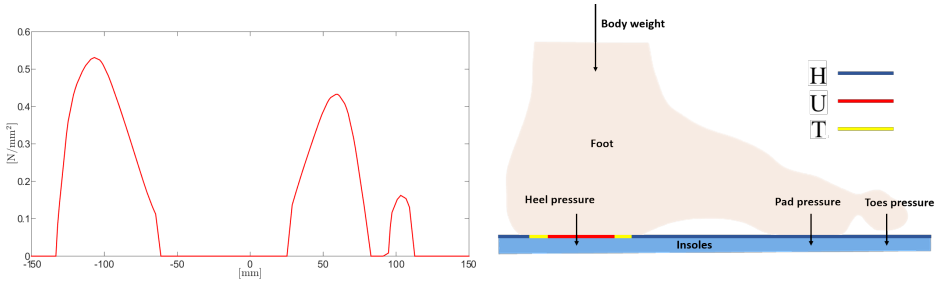

Figure 4: Patient-specific design of an orthopedic device: load distribution (left) and location of the healthy, ulcerated and pre-ulcerated areas (right).

selected in order to minimize the stress component along the vertical direction on the patient's foot.

6.1.1 Insole optimization based on the single-cellular dictionary

To design the orthopedic device by means of a graded single topology, we resort to Algorithm 3 with the input parameters

$$\mathcal{D} = \mathcal{D}_{\mathrm{S}}, \quad \texttt{TOPT} = \texttt{1e-06}, \quad \rho_{\min} = 0.35, \quad \rho_{\max} = 0.9,$$

$\mathbf{c}_m$, $\mathbf{c}_M$ to be properly set according to the selected H-U or H-U-T configuration, $\rho^0_{M,h} = 0.95\chi_\Omega$, with χ_Ω the characteristic function associated with domain Ω, and where $\mathcal{D}_{\mathrm{S}}$ is the single-cellular dictionary in Figure 1.

As a first task, Algorithm 3 performs the fitting of the data $\{\alpha_s, E^H_{ijkl,\tau_s}\}_{s=1,\dots,8}$, for $ijkl = 1111$, 2222, 1122, 1212, the components E^H_{1112,τ_s} E^H_{2212,τ_s} being identically null, and the full material configuration being added to the ones in Figure 1 for $s = 8$. To this aim, we adopt a global polynomial least-square approximation of degree n. The value $n = 5$ is the lowest degree which provides us a sufficiently reliable data approximation. In particular, Figure 5 shows the plot of the polynomials $\Phi^H_{ijkl}(\alpha)$, where the circle markers highlight the fitted values for the homogenized tensor components. The four curves ensure tensor $\Xi^H(\rho_M)$ to be well-defined as a function of ρ_M. Additionally, we have numerically checked that tensor Ξ^H is definite positive for any ρ_M, which implies that the bilinear form $a^H_{\rho_M}(\cdot,\cdot)$ in (28) is coercive.

The fitting in Figure 5 becomes instrumental to function `optimize` of Algorithm 3, since, via (29), it defines the PDE problem constraining the topology optimization in (27).
The lower and the upper bound for the two-sided constraint in (27) are set to

$$\mathbf{c}_m = [5.50, 15.00]^T, \quad \mathbf{c}_M = [7.50, 17.00]^T,$$

and

$$\mathbf{c}_m = [7.00, 15.00, 8.50]^T, \quad \mathbf{c}_M = [8.00, 15.50, 9.00]^T,$$

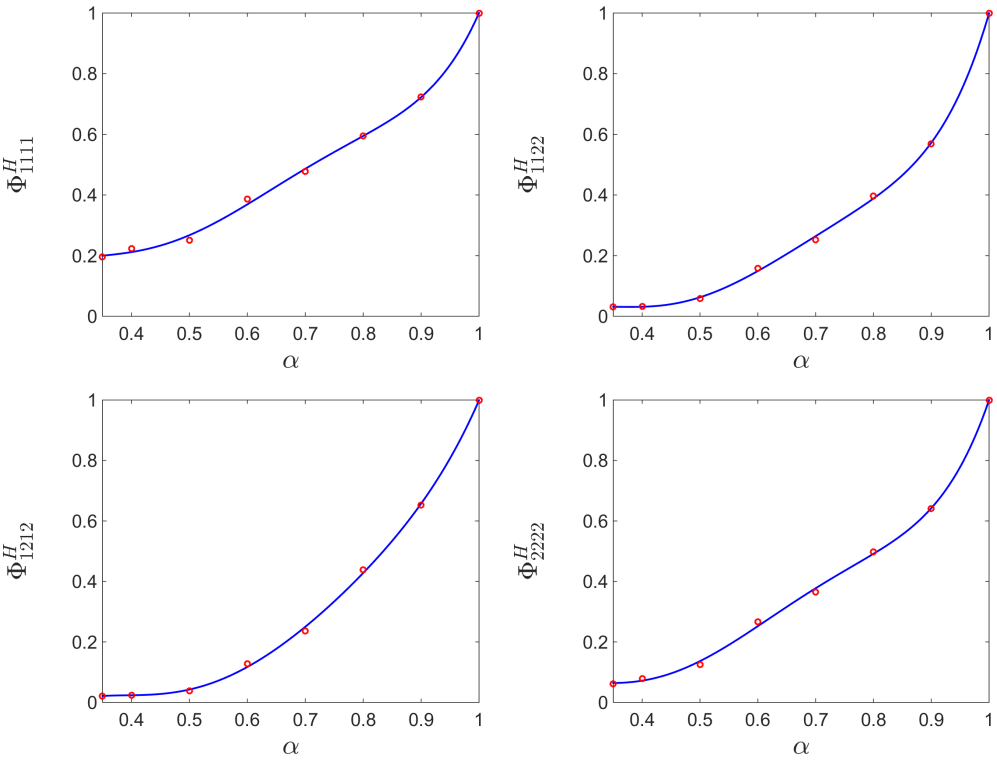

Figure 5: Optimized insole (single-cellular dictionary): fitting of the homogenized stiffness tensor components.

for the H-U and the H-U-T scenario, respectively corresponding to a requirement of high and low (and, if included, medium) stiffness for the insole.

The distribution of the multiscale density function $\rho_{M,h}$ representing the output of Algorithm 3 is shown in Figure 6 for the patient-specific H-U (top) and H-U-T (bottom) setting. The presence of the transition area between healthy and ulcerated zones induces a milder gradation of the material density in correspondence with the sick and the loaded portions of the boundary Γ_N. The total mass of the two insoles is given by 37.8% and 39.4% of the full material configuration for the H-U and the H-U-T scenario, respectively.

In order to grade the different unit cells across the optimized insole, we exploit again the relationship between $\rho_{M,h}$ at the homogenized macroscale and α at the microscale. In particular, we resort to a thresholding of $\rho_{M,h}$ to identify the different subregions, ω_s, of the design domain associated with a specific microscopic layout, τ_s. The number of the subregions ω_s will be, at most, equal to $z+1$, after assuming that the full material configuration corresponds to $s = z+1$.
According to the thresholding criterion here adopted, we define the subregions

$$\omega_s = \{\mathbf{x} \in \Omega : \alpha_s + \delta_{l,s} \leq \rho_{M,h}(\mathbf{x}) = \alpha < \alpha_{s+1} + \delta_{u,s}\}$$

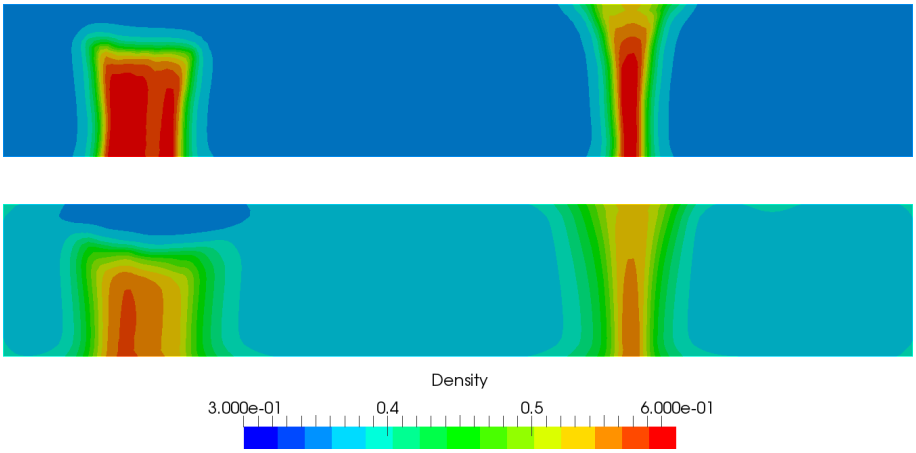

Figure 6: Optimized insole (single-cellular dictionary): optimized distribution of the density $\rho_{M,h}$ for the patient-specific H-U (top) and H-U-T (bottom) configuration.

for $s = 1, \dots, z$, with $\delta_{l,s}$, $\delta_{u,s} \in \mathbb{R}$ properly selected by the user according to the density distribution range, and region

$$\omega_{z+1} = \{\mathbf{x} \in \Omega : \rho_{M,h}(\mathbf{x}) = \alpha \geq 1 - \delta_{z+1}\},$$

being $\delta_{z+1} \in \mathbb{R}^+$ set by the user.
By applying this thresholding to the configurations in Figure 6, we obtain the four subregions ω_i, with $i = 1, \dots, 4$, shown in Figure 7, after setting $\delta_{l,1} = 0$, $\delta_{u,1} = \delta_{l,2} = -0.025$, $\delta_{u,2} = \delta_{l,3} = \delta_{u,4} = -0.05$, $\delta_{u,3} = \delta_{l,4} = -0.065$. We observe that the inclusion of the pre-ulcerated area in the insole design introduces an area of soft material just below the ulcer, and promotes the intermediate densities corresponding to the volume fractions $\alpha = 0.4$ and $\alpha = 0.5$. These results support not only the reduction of pressure below the ulcerated area but confirm the need of a pressure re-distribution around those areas.

6.1.2 Insole optimization based on the multi-cellular dictionary

The topology optimization of the insole is now driven by exploiting the multi-cellular dictionary $\mathcal{D}_{\mathtt{M}}$ generated in Section 4.2. To this aim, we run Algorithm 3 with the input parameters

$$\mathcal{D} = \mathcal{D}_{\mathtt{M}}, \quad \mathtt{TOPT} = \mathtt{1e-06}, \quad \rho_{\min} = 0.2, \quad \rho_{\max} = 0.7,$$

while selecting

$$\mathbf{c}_m = [18.50, 38.50]^T, \quad \mathbf{c}_M = [20.50, 39.00]^T.$$

for the H-U setting,

$$\mathbf{c}_m = [17.00, 38.50, 24.00]^T, \quad \mathbf{c}_M = [18.00, 39.00, 25.00]^T.$$

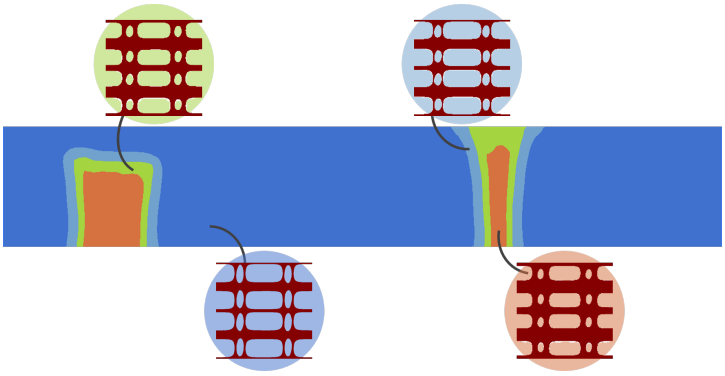

(a) H-U scenario

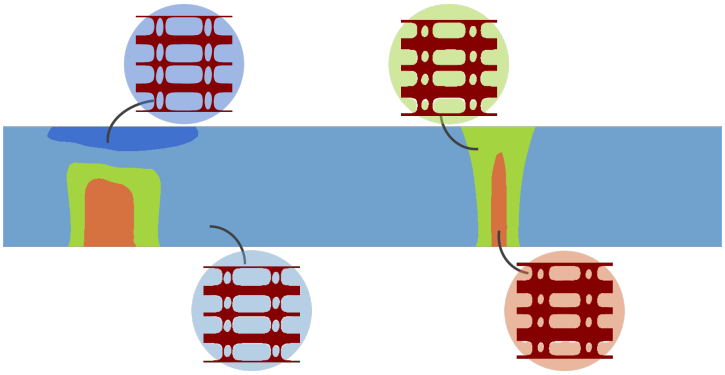

(b) H-U-T scenario

Figure 7: Optimized insole (single-cellular dictionary): allocation of the different unit cells across the insole.

for the H-U-T configuration, and with $\rho^0_{M,h} = 0.95\chi_\Omega$.

The fitting of the homogenized stiffness tensor components E^H_{ijkl,τ_s} as a function of the density α is carried out, for $s = 1,\dots,10$ where $s = 10$ identifies the full material unit cell, by employing a polynomial of degree $n = 5$, approximating the data according to a least-squares criterion. Figure 8 gathers the polynomials $\Phi^H_{ijkl}(\alpha)$ together with the data to be approximated. A cross-comparison with Figure 5 shows that the four curves exhibit a similar trend, except for polynomial Φ^H_{1111} which increases slower to 1 when dealing with the multi-cellular dictionary.

The output of Algorithm 3 coincides with the distribution of $\rho_{M,h}$ in Figure 9, where the optimal design of the insole is distinguished between the H-U and the H-U-T scenarios (top and bottom, respectively). The distribution of the material density is very similar, although the presence of the pre-ulcerated area leads to a wider extension of the subdomains corresponding to $\alpha = 0.4$. This justifies the slight difference in the total mass of the insole for the H-U and H-U-T settings, equal to

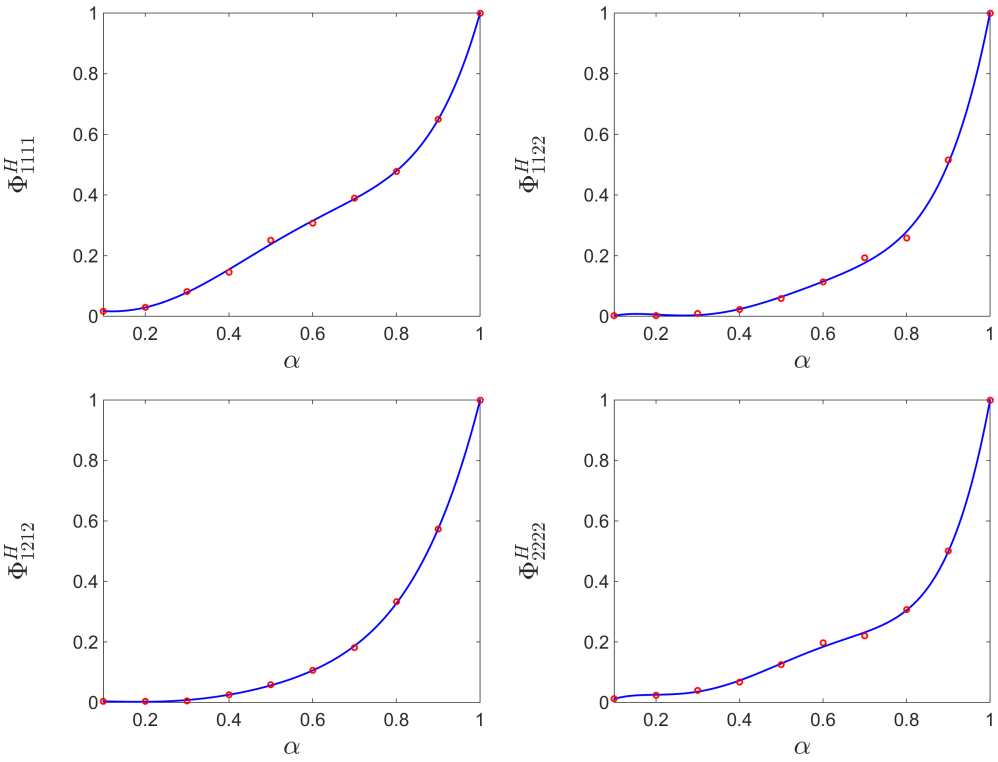

Figure 8: Optimized insole (multi-cellular dictionary): fitting of the homogenized stiffness tensor components.

29.8% and 32.4% of the full material domain, respectively. Moreover, the ulcer is taken into account in both the H-U and H-U-T designs in contrast to Figure 6 (top panel) where the same density characterizes the ulcerated and the healthy portions.

With a view to the manufacturing of the optimized insoles in Figure 9, we apply the thresholding procedure introduced in the previous section. This strategy leads us to identify three subregions, ω_2, ω_3, ω_4, for both the scenarios, H-U and H-U-T, after selecting $\delta_{l,2} = 0$, $\delta_{l,3} = \delta_{l,4} = \delta_{u,s} = -0.05$ for $s = 2,3,4$. Figure 10 shows the distribution of the three regions together with the associated unit cells.

When compared with the single-cellular case (see Figure 7), we recognize that the multi-cellular dictionary involves fewer unit cells in the prototype of the insole and turns out to be less sensitive to the inclusion of the pre-ulcerated zone in the design of the orthotic device.

Finally, the two panels in Figure 10 emphasize that the presence of the transition area between the healthy and the ulcerated tissue increases the extension of region ω_4 associated with the volume fraction $\alpha = 0.4$. The transition areas favour the re-distribution of the pressure, thus avoiding undesired localization of the load.

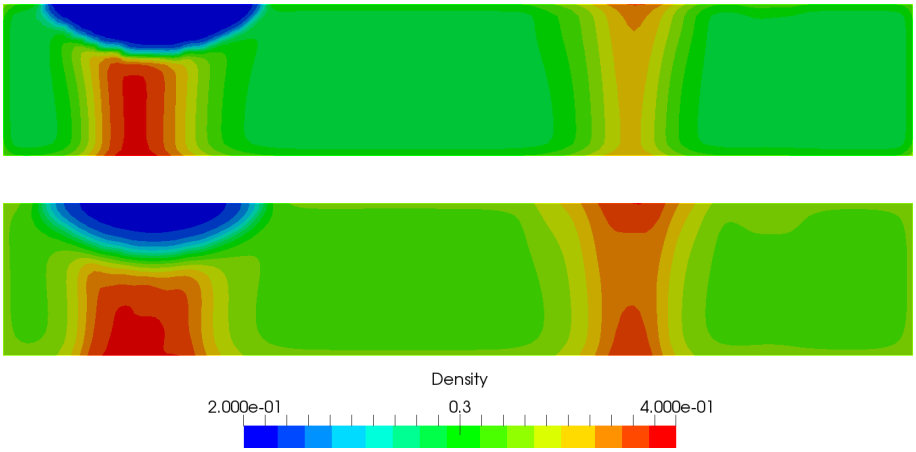

Figure 9: Optimized insole (multi-cellular dictionary): optimized distribution of the density $\rho_{M,h}$ for the patient-specific H-U (top) and H-U-T (bottom) configuration.

6.2 Validation

The optimization procedure set for the design of othopedic devices is finally tested in practice via a mechanical validation, in the case of the patient-specific H-U-T configuration of Figure 10. In detail, we computationally explore the macroscopic mechanical behaviour of the prototype via a finite element analysis. Then, we investigate the 3D printing manufacturability of the design, via fused deposition modelling (FDM).

6.2.1 Mechanical performance evaluation

For the finite element analysis, we refer to the 2D geometry in Figure 11, where the insole is regarded as a porous continuum body and includes a thin layer on the top, to simulate the foot tissue (i.e., fat and skin) in contact with the orthotic device. To evaluate the mechanical performance of the optimized insole, we assume as the reference case the behaviour characterizing the H-U-T configuration when resorting to a standard honeycomb design. In more detail, we mechanically test three insole settings, i.e., (1) honeycomb design with constant volume fraction of 30%; (2) honeycomb design with variable volume fraction, with the same distribution as in Figure 10, panel (b); (3) the optimized H-U-T configuration in Figure 10, panel (b).

The foot tissue layer is assumed linearly elastic, homogeneous and isotropic as well as the mechanical behaviour of the Thermoplastic Polyether-polyurethane Elastomer (TPE) material composing the insole, with Young's modulus and Poisson's ratio equal to $E_{TPE} = 45$ [MPa], $\nu_{TPE} = 0.49$, respectively. For the foot tissue, we set $E_{foot} = 1$ [MPa], $\nu_{foot} = 0.4$. The loading condition applied to the top tissue

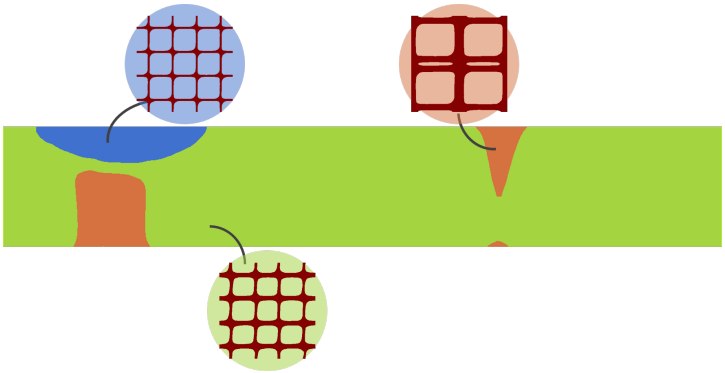

(a) H-U scenario

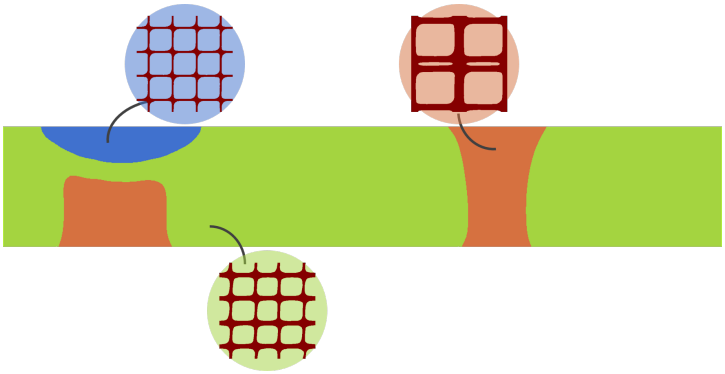

(b) H-U-T scenario

Figure 10: Optimized insole (multi-cellular dictionary): allocation of the different unit cells across the insole.

layer coincides with the patient-specific load distribution in Figure 4, left, while the bottom boundary of the insole is constrained, as shown in Figure 11.

The mechanical analysis for cases (1)-(3) is carried out by using the software COMSOL Multiphysics[3]. Figure 12 compares the deformation of the three designs under the imposed load, in terms of spatial distribution of the displacement magnitude. It is evident that the three insoles exhibit a different mechanical behaviour. In particular, the optimized configuration yielded by the procedure in Section 6.1.2 exhibits a maximum value for the displacement which is 2 and 3 times lower with respect to the one characterizing designs (1) and (2), respectively. This is confirmed by Figure 13, left which shows the displacement profile along the cut line highlighted by the black dashed line in Figure 11. It is evident that the new designed configuration localizes and attenuates the displacement in the ulcer zone, thus preventing the stress concentration in the surrounding area.

[3]COMSOL Multiphysics®. Version 5.6, www.comsol.com, COMSOL AB, Stockholm, Sweden

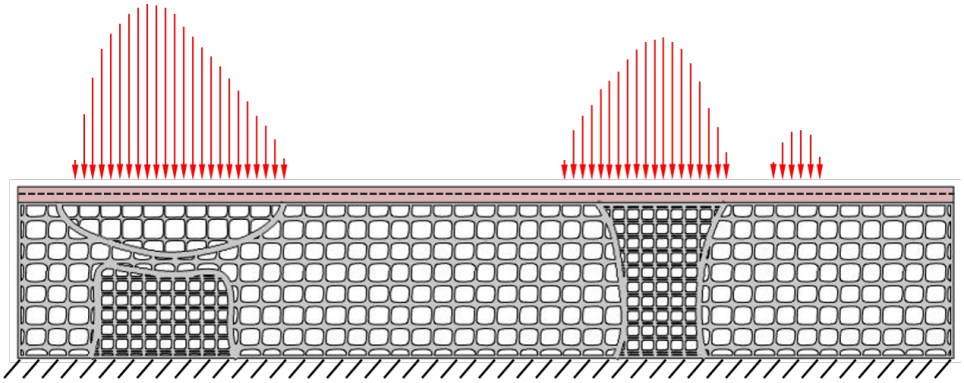

Figure 11: Optimized insole (mechanical validation): schematic representation for the H-U-T configuration.

In order to characterize the loading-transfer mechanism between insole and foot tissue, in Figure 13, right, we investigate the mechanical behaviour of the three designs in terms of the von Mises stress distribution along the same cut line as in Figure 11. The optimized layout in Figure 10, (b) dampens the stress in the foot tissue and localizes the effect of the loading pressure. In particular, when employing the two honeycomb insoles, the pressure affects also the plantar arch zone (i.e., the region between 0.1 and 0.15 [m]), though this area is not loaded. This is not the case for the multi-cellular dictionary in Figure 2, thus introducing an innovative and relevant advantage in the design of orthopedic insoles.

6.2.2 Manufacturing feasibility evaluation

To assess the feasibility of the orthopedic device in Figure 10, (b) in terms of manufacturing, we apply an axial extrusion of 0.01 [m] to the optimized insole in Figure 11, in order to obtain a section of the 3D model. To this aim, we use the dedicated software of slicing, Simplify3D[4], to generate a g-code for the 3D printer. The flexible TPE filament Filaflex, with a shore A equal to 82 (Filaflex 82A), has been selected to manufacture the extruded section shown in Figure14. This material has proved to be suitable for the 3D printing of insoles, since it has an optimal resistance to elongation and abrasion as well as a high tensile strength [15]. These properties make Filaflex 82A a perfect material for the production of flexible, comfortable and resistant insoles.
Different slicing parameters and profiles have been tested to obtain an optimal result in terms of reliability and quality of production. After several tests, the main printing parameters are set as: print speed 2200 [mm/min], extruder temperature 235 [°C], cooling 60%, no-retraction, top/bottom/outline perimeters equal to 3. The model took approximately 10 hours of printing.

These preliminary results confirm the feasibility of the proposed method to create

[4]Symplify3D®. Version 4.0, www.simplify3d.com

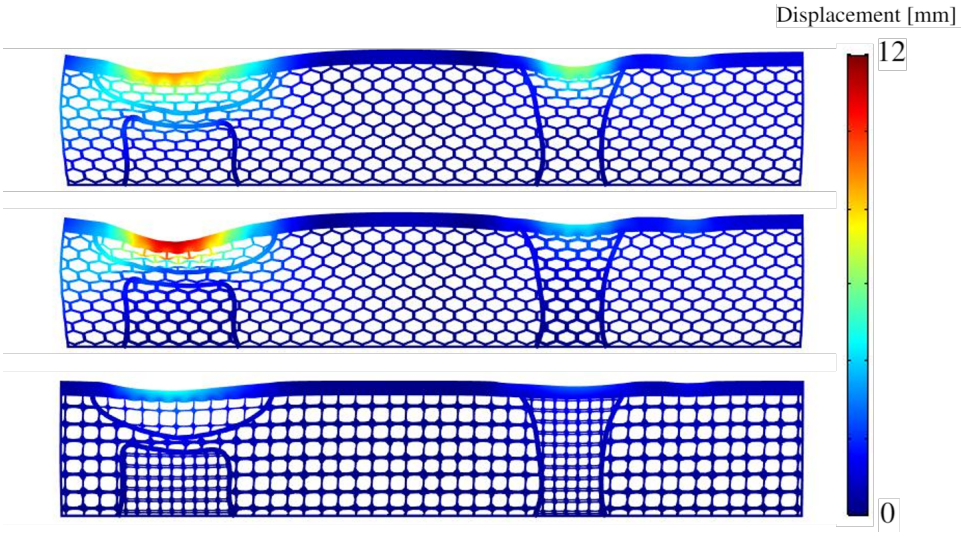

Figure 12: Optimized insole (mechanical validation): spatial distribution of the displacement magnitude for the insole settings (1)-(3) (top-bottom).

innovative and patient-specific solution for foot problems. The different areas are well defined and the process was reasonable in terms of printing time and overall quality. This is a promising starting point for the realisation of a full model of patient-specific insoles that can be used for prevention of ulceration and can lead to a better medical outcome.

7 Conclusions

The multiscale topology optimization proposed in this paper provides a fully general, cost-effective tool for the design of macrostructures optimized in terms of

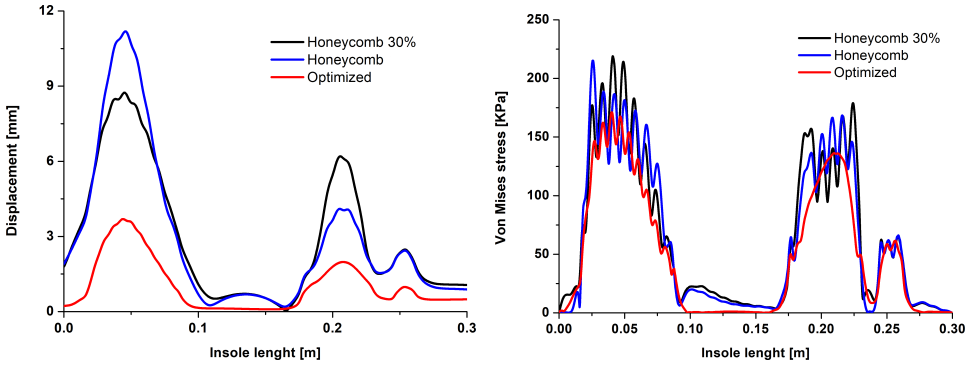

Figure 13: Optimized insole (mechanical validation): displacement magnitude (left) and von Mises stress (right) profiles for the insole settings (1)-(3).

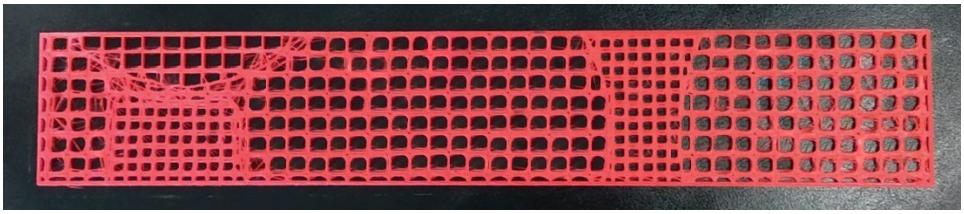

Figure 14: Optimized insole (3D printing validation): manufacturing of the section of the orthopedic prototype in Figure 11.

local distribution of void, solid, and cellular materials. Among the relevant properties, we list the possibility to decouple the optimization at the macro- and at the microscale, possibly associated with different goal functionals. This feature allows us to control target quantities which are simultaneously pivotal in the design of the final product, in the spirit of a multi-objective optimization. Moreover, the non concurrent optimizations at the micro- and at the macroscale lighten the computational burden of the whole procedure. Indeed, the generation of the cell dictionary could be, a priori, confined to a preliminary phase, mimicking an offline/online paradigm.

A cross-comparison between the single-cellular and the multi-cellular dictionary optimization, customized to the design of orthotic devices, represents another interesting contribution of the paper. Actually, the possibility to involve different topologies in the design of the optimized macrostructure results in the adoption of a lower number of different unit cells, i.e., in a structure simpler to be manufactured. Additionally, the multi-cellular dictionary admits very small volume fractions (for instance, values $\alpha = 0.2, 0.3$ excluded by $\mathcal{D}_S$) which are used in practice to finalize the optimized layout in Figure 10. Moreover, dictionary $\mathcal{D}_M$ seems to be less sensitive with respect to the two analyzed patient-specific configurations. Indeed, the presence of the pre-ulcerated area in Figure 10 essentially preserves the allocation of the unit cells when compared with the H-U scenario, just slightly increasing the extension of the zones associated with the highest density. This is in contrast to the optimized layouts in Figure 7 associated with the single-cellular dictionary, which strongly differ in the global unit cells distribution and in the presence of a soft region just below the damaged area in the H-U-T configuration.

The validation carried out in Section 6.2 confirms that the developed multiscale topology optimization can lead to some benefits when compared with consolidated medical practices. In particular, the finite element analysis in Figure 13 shows that the insole design in Figure 10 for the H-U-T scenario reduces the stress in correspondence with the ulcerated zone and the plantar arch, when compared with standard homogeneous and heterogeneous honeycomb infills. Finally, the manufacturing analysis in Section 6.2.2 confirms the feasibility of the optimized prototype with respect to a 3D printing technology.
These preliminary results support the proposed multiscale topology optimization as

an effective computational and manufacturing workflow for the design of custom-made insoles for specific foot pathologies.

As a first possible development, we plan to extend the methodology here presented to a 3D setting to provide a more effective solution to different foot pathologies and to comply with patient-specific clinical prescriptions.
In addition, both the optimization phases can be enriched with constraints taking into account the current limits in additive manufacturing [18, 44, 45, 75, 80, 95, 104], as well as the presence of possible failures or geometric defects [62] in the final layouts.
A handy management of the transition between different cell layouts represents another crucial issue with a view to manufacturability, in particular when dealing with heterogeneous dictionaries.
A multi-physics optimization, where different physical problems coexist, turns out to be another further step towards a more comprehensive description of complex phenomena.

References

[1] Ahmed S, Barwick A, Butterworth P, Nancarrow S (2020) Footwear and insole design features that reduce neuropathic plantar forefoot ulcer risk in people with diabetes: a systematic literature review. J Foot Ankle Res 13:1–13

[2] Ainsworth M, Oden JT (2000) A Posteriori Error Estimation in Finite Element Analysis. John Wiley & Sons, New York

[3] Alaimo G, Auricchio F, Conti M, Zingales M (2017) Multi-objective optimization of nitinol stent design. Med Eng Phys 47:13–24

[4] Alaimo G, Auricchio F, Bianchini I, Lanzarone E (2018) Applying functional principal components to structural topology optimization. Internat J Numer Methods Engrg 115(2):189–208

[5] Allaire G, Jouve F, Maillot H (2004) Topology optimization for minimum stress design with the homogenization method. Struct Multidisc Optim 28:87–98

[6] Allaire G, Jouve F, Toader A (2004) Structural optimization using sensitivity analysis and level set-method. J Comput Phys 194:363–393

[7] Allaire G, Geoffroy-Donders P, Pantz O (2019) Topology optimization of modulated and oriented periodic microstructures by the homogenization method. Comput Math Appl 78(7):2197–2229

[8] Andreassen E, Andreasen CS (2014) How to determine composite material properties using numerical homogenization. Comp Mater Sci 83:488–495

[9] Arabnejad Khanoki S, Pasini D (2012) Multiscale design and multiobjective

optimization of orthopedic hip implants with functionally graded cellular material. J Biomech Eng 134(3):031004

[10] Auricchio F, Bonetti E, Carraturo M, Hömberg D, Reali A, Rocca E (2020) A phase-field-based graded-material topology optimization with stress constraint. Math Models Methods Appl Sci 30(8):1461–1483

[11] Belhamadia Y, Fortin A, Bourgault Y (2014) On the performance of anisotropic mesh adaptation for scroll wave turbulence dynamics in reaction-diffusion systems. J Comput Appl Math 271:233–246

[12] Bendsøe MP (1995) Optimization of Structural Topology, Shape, and Material. Springer-Verlag, Berlin

[13] Bendsøe MP, Kikuchi N (1988) Generating optimal topologies in structural design using a homogenization method. Comput Methods Appl Mech Engrg 71(2):197–224

[14] Bendsøe MP, Sigmund O (2003) Topology Optimization: Theory, Methods and Applications. Springer-Verlag, Berlin Heidelberg

[15] Bianchi D, Mannisi M (2019) Pop project. URL https://medere.it/en/our-projects/

[16] Borrvall T, Petersson J (2003) Topology optimization of fluids in Stokes flow. Internat J Numer Methods Fluids 41(1):77–107

[17] Bourdin B, Chambolle A (2003) Design-dependent loads in topology optimization. ESAIM Control Optim Calc Var 9:19–48

[18] Brackett D, Ashcroft I, Hague R (2011) Topology optimization for additive manufacturing. In: Proceedings of the Solid Freeform Fabrication Symposium, Austin, TX, S, vol 1, pp 348–362

[19] Bruggi M, Corigliano A (2019) Optimal 2D auxetic micro-structures with band gap. Meccanica 54(13):2001–2027

[20] Bruggi M, Verani M (2011) A fully adaptive topology optimization algorithm with goal-oriented error control. Comput Struct 89(15-16):1481–1493

[21] Challis V, Roberts A, Wilkins A (2008) Design of three dimensional isotropic microstructures for maximized stiffness and conductivity. Int J Solids Struct 45(14-15):4130–4146

[22] Chatzistergos PE, Naemi R, Healy A, Gerth P, Chockalingam N (2017) Subject specific optimisation of the stiffness of footwear material for maximum plantar pressure reduction. Ann Biomed Eng 45(8):1929–1940

[23] Chi H, Zhang Y, Tang TLE, Mirabella L, Dalloro L, Song L, Paulino GH (2021) Universal machine learning for topology optimization. Comput Methods Appl Mech Engrg 375:112739, 35

[24] Coelho PG, Fernandes PR, Guedes JM, Rodrigues HC (2008) A hierar-

chical model for concurrent material and topology optimisation of three-dimensional structures. Struct Multidiscipl Optim 35(2):107–115

[25] Collings R, Freeman J, Latour JM, Paton J (2021) Footwear and insole design features for offloading the diabetic at risk foot—a systematic review and meta-analyses. Endocrinol Diabetes Metab 4(1):e00132

[26] di Cristofaro D, Galimberti C, Bianchi D, Ferrante R, Ferro N, Mannisi M, Perotto S (2021) Adaptive topology optimization for innovative 3D printed metamaterials. In: Proceedings of WCCM – ECCOMAS 2020 Conference, Volume 1200 - Modeling and Analysis of Real World and Industry Applications.

[27] Dapogny C, Faure A, Michailidis G, Allaire G, Couvelas A, Estevez R (2017) Geometric constraints for shape and topology optimization in architectural design. Comput Mech 59(6):933–965

[28] Dedè L, Borden MJ, Hughes TJR (2012) Isogeometric analysis for topology optimization with a phase field model. Arch Comput Methods Eng 19(3):427–465

[29] Dompierre J, Vallet MG, Bourgault Y, Fortin M, Habashi WG (2002) Anisotropic mesh adaptation: towards user-independent, mesh-independent and solver-independent CFD. III. Unstructured meshes. Internat J Numer Methods Fluids 39(8):675–702

[30] Du Z, Zhou XY, Picelli R, Kim HA (2018) Connecting microstructures for multiscale topology optimization with connectivity index constraints. J Mech Des 140(11):111417

[31] Ern A, Guermond JL (2004) Theory and Practice of Finite Elements, Applied Mathematical Sciences, vol 159. Springer-Verlag, New York

[32] Farrell PE, Micheletti S, Perotto S (2011) An anisotropic Zienkiewicz-Zhu-type error estimator for 3D applications. Int J Numer Meth Engng 85(6):671–692

[33] Ferro N, Micheletti S, Perotto S (2018) Anisotropic mesh adaptation for crack propagation induced by a thermal shock in 2D. Comput Methods Appl Mech Engrg 331:138–158

[34] Ferro N, Micheletti S, Perotto S (2019) POD-assisted strategies for structural topology optimization. Comput Math Appl 77(10):2804–2820

[35] Ferro N, Micheletti S, Perotto S (2020) Compliance–stress constrained mass minimization for topology optimization on anisotropic meshes. SN Applied Sciences 2:1196

[36] Ferro N, Micheletti S, Perotto S (2020) Density-based inverse homogenization with anisotropically adapted elements. In: Corsini A, Perotto S, Rozza G, van Brummelen H (eds) Numerical Methods for Flows, Lect. Notes Com-

put. Sci. Eng., vol 132, Springer Cham, pp 211–221

[37] Ferro N, Micheletti S, Perotto S (2020) An optimization algorithm for automatic structural design. Comput Methods Appl Mech Engrg 372:113335

[38] Fiedler K, Rolfe BF, Souza TD (2017) Integrated shape and topology optimization - applications in automotive design and manufacturing. SAE Int J Mater Manuf 10(3):385–394

[39] Formaggia L, Perotto S (2001) New anisotropic a priori error estimates. Numer Math 89(4):641–667

[40] Formaggia L, Micheletti S, Perotto S (2002) Anisotropic mesh adaption with application to CFD problems. In: Mang H, Rammerstorfer F, Eberhardsteiner J (eds) Proceedings of WCCM V, Fifth World Congress on Computational Mechanics, pp 1481–1493

[41] Gao J, Luo Z, Li H, Gao L (2019) Topology optimization for multiscale design of porous composites with multi-domain microstructures. Comput Methods Appl Mech Engrg 344:451–476

[42] Gao T, Xu P, Zhang W (2016) Topology optimization of thermo-elastic structures with multiple materials under mass constraint. Comput Struct 173:150–160

[43] Garcke H, Hecht C, Hinze M, Kahle C (2015) Numerical approximation of phase field based shape and topology optimization for fluids. SIAM J Sci Comput 37(4):A1846–A1871

[44] Gardan J (2016) Additive manufacturing technologies: state of the art and trends. Int J Prod Res 54(10):3118–3132

[45] Giraldo-Londoño O, Mirabella L, Dalloro L, Paulino GH (2020) Multimaterial thermomechanical topology optimization with applications to additive manufacturing: design of main composite part and its support structure. Comput Methods Appl Mech Engrg 363:112812

[46] Griffith L, Raina P, Wu H, Zhu B, Stathokostas L (2010) Population attributable risk for functional disability associated with chronic conditions in Canadian older adults. Age Ageing 39(6):738–745

[47] Groen JP, Sigmund O (2018) Homogenization-based topology optimization for high-resolution manufacturable microstructures. Int J Numer Meth Engng 113(8):1148–1163

[48] Hecht F (2012) New development in FreeFem++. J Numer Math 20(3-4):251–265

[49] Helnwein P (2001) Some remarks on the compressed matrix representation of symmetric second-order and fourth-order tensors. Comput Methods Appl Mech Engrg 190(22-23):2753–2770

[50] Hsu YS (2021) A hierarchically enhanced recovery-based error estimator for bidimensional elastoplastic modelling by generalized finite element approach. Acta Mech 232(3):881–906

[51] Huang X, Radman A, Xie Y (2011) Topological design of microstructures of cellular materials for maximum bulk or shear modulus. Comput Mater Sci 50(6):1861–1870

[52] Iseli RK, Lee EK, Lewis E, Duncan G, Maier AB (2021) Foot disease and physical function in older adults: a systematic review and meta-analysis. Australas J Ageing 40(1):35–47

[53] Ivarsson N, Wallin M, Tortorelli DA (2020) Topology optimization for designing periodic microstructures based on finite strain viscoplasticity. Struct Multidiscip Optim 61(6):2501–2521

[54] Jenkins N, Maute K (2016) An immersed boundary approach for shape and topology optimization of stationary fluid-structure interaction problems. Struct Multidiscip Optim 54(5):1191–1208

[55] Jeong SH, Choi DH, Yoon GH (2015) Fatigue and static failure considerations using a topology optimization method. Appl Math Model 39(3):1137–1162

[56] Karia S, Parasuraman S, Khan MA, Elamvazuthi I, Debnath N, Ali SSA (2016) Plantar pressure distribution and gait stability: normal vs high heel. In: 2016 2nd IEEE International Symposium on Robotics and Manufacturing Automation (ROMA), IEEE, pp 1–5

[57] Kiziltas G, Kikuchi N, Volakis JL, Halloran J (2004) Topology optimization of dielectric substrates for filters and antennas using SIMP. Arch Comput Methods Eng 11(4):355–388

[58] Kunisch K, Volkwein S (2002) Galerkin proper orthogonal decomposition methods for a general equation in fluid dynamics. SIAM J Numer Anal 40(2):492–515

[59] Lazzarini PA, Hurn SE, Kuys SS, Kamp MC, Ng V, Thomas C, Jen S, Wills J, Kinnear EM, d'Emden MC, Reed LF (2017) The silent overall burden of foot disease in a representative hospitalised population. Int Wound 14(4):716–728

[60] Liang Q (2005) Performance-based Optimization of Structures. Theory and Applications. Spon Press, London

[61] Lions JL (1971) Optimal Control of Systems Governed by Partial Differential Equations. Springer-Verlag, New York-Berlin

[62] Liu L, Kamm P, García-Moreno F, Banhart J, Pasini D (2017) Elastic and failure response of imperfect three-dimensional metallic lattices: the role of geometric defects induced by selective laser melting. J Mech Phys Solids

107:160–184

[63] López-López D, Becerro-de Bengoa-Vallejo R, Losa-Iglesias ME, Palomo-López P, Rodríguez-Sanz D, Brandariz-Pereira JM, Calvo-Lobo C (2018) Evaluation of foot health related quality of life in individuals with foot problems by gender: a cross-sectional comparative analysis study. BMJ Open 8(10):e023980

[64] Loseille A, Dervieux A, Alauzet F (2010) Fully anisotropic goal-oriented mesh adaptation for 3D steady Euler equations. J Comput Phys 229(8):2866–2897

[65] M Wang XW, Guo D (2003) A level set method for structural topology optimization. Comput Methods Appl Mech Eng 192(1-2):227–246

[66] Mannisi M, Dell'Isola A, Andersen MS, Woodburn J (2019) Effect of lateral wedged insoles on the knee internal contact forces in medial knee osteoarthritis. Gait Posture 68:443–448

[67] Mello LAM, Salas RA, Silva ECN (2012) On response time reduction of electrothermomechanical MEMS using topology optimization. Comput Methods Appl Mech Engrg 247-248:93–102

[68] Menz HB, Auhl M, Spink MJ (2018) Foot problems as a risk factor for falls in community-dwelling older people: a systematic review and meta-analysis. Maturitas 118:7–14

[69] Micheletti S, Perotto S (2006) Reliability and efficiency of an anisotropic Zienkiewicz-Zhu error estimator. Comput Methods Appl Mech Engrg 195(9–12):799–835

[70] Micheletti S, Perotto S (2010) Anisotropic adaptation via a Zienkiewicz-Zhu error estimator for 2D elliptic problems. In: Kreiss G, Lötstedt P, Målqvist A, Neytcheva M (eds) Numerical Mathematics and Advanced Applications, Springer-Verlag Berlin Heidelberg, pp 645–653

[71] Micheletti S, Perotto S, Farrell PE (2010) A recovery-based error estimator for anisotropic mesh adaptation in CFD. Bol Soc Esp Mat Apl SeMA 50:115–137

[72] Micheletti S, Perotto S, Soli L (2019) Topology optimization driven by anisotropic mesh adaptation: towards a free-form design. Comput Struct 214:60 – 72

[73] Michell AGM (1904) The limits of economy of material in frame-structures. The London, Edinburgh, and Dublin Philosophical Magazine and Journal of Science 8(47):589–597

[74] Molter A, Fonseca JSO, dos Santos Fernandez L (2016) Simultaneous topology optimization of structure and piezoelectric actuators distribution. Appl Math Model 40(9):5576–5588

[75] Moussa A, Rahman S, Xu M, Tanzer M, Pasini D (2020) Topology optimization of 3D-printed structurally porous cage for acetabular reinforcement in total hip arthroplasty. J Mech Behav Biomed Mater 105:103705

[76] Mu L, Jari R (2013) A recovery-based error estimate for nonconforming finite volume methods of interface problems. Appl Math Comput 220:63–74

[77] Nakshatrala PB, Tortorelli DA, Nakshatrala KB (2013) Nonlinear structural design using multiscale topology optimization. Part I: static formulation. Comput Methods Appl Mech Engrg 261/262:167–176

[78] Noël L, Duysinx P (2017) Shape optimization of microstructural designs subject to local stress constraints within an XFEM-level set framework. Struct Multidiscip Optim 55(6):2323–2338

[79] Pizzolato A, Sharma A, Maute K, Sciacovelli A, Verda V (2017) Topology optimization for heat transfer enhancement in latent heat thermal energy storage. Int J Heat Mass Transf 113:875–888

[80] Plocher J, Panesar A (2019) Review on design and structural optimisation in additive manufacturing: towards next-generation lightweight structures. Mater Des 183:108164

[81] Porta GM, Perotto S, Ballio F (2012) Anisotropic mesh adaptation driven by a recovery-based error estimator for shallow water flow modeling. Internat J Numer Methods Fluids 70(3):269–299

[82] Radman A, Huang X, Xie YM (2013) Topology optimization of functionally graded cellular materials. J Mater Sci 48(4):1503–1510

[83] Rodrigues H, Guedes J, Bendsoe M (2002) Hierarchical optimization of material and structure. Struct Multidiscip Optim 24(1):1–10

[84] Rozvany GIN (1972) Grillages of maximum strength and maximum stiffness. Int J Mech Sci 14(10):651–666

[85] Rozvany GIN (2009) A critical review of established methods of structural topology optimization. Struct Multidiscip Optim 37:217–237

[86] Rozvany GIN (2012) Structural design via optimality criteria: the Prager approach to structural optimization, Mechanics of Elastic and Inelastic Solids, vol 8. Springer Netherlands

[87] Sibileau A, García-González A, Auricchio F, Morganti S, Díez P (2018) Explicit parametric solutions of lattice structures with proper generalized decomposition (PGD): applications to the design of 3D-printed architectured materials. Comput Mech 62(4):871–891

[88] Sigmund O (1994) Materials with prescribed constitutive parameters: an inverse homogenization problem. Internat J Solids Structures 31(17):2313–2329

[89] Sigmund O, Maute K (2013) Topology optimization approaches, a comparative review. Struct Multidiscip Optim 48(6):1031–1055

[90] Sigmund O, Petersson J (1998) Numerical instabilities in topology optimization: a survey on procedures dealing with checkerboards, mesh-dependencies and local minima. Struct Optim 16(1):68–75

[91] Sokolowski J, Zochowski A (1999) On the topological derivative in shape optimization. SIAM J Control Opt 37:1251–1272

[92] Sun Y, Liu Y, Xu L, Lueth TC (2019) Design of a disposable compliant medical forceps using topology optimization techniques. In: 2019 IEEE International Conference on Robotics and Biomimetics (ROBIO), pp 924–929

[93] Svanberg K (1987) The method of moving asymptotes-a new method for structural optimization. Int J Numer Meth Engng 24(2):359–373

[94] Telfer S, Woodburn J, Collier A, Cavanagh P (2017) Virtually optimized insoles for offloading the diabetic foot: a randomized crossover study. J Biomech 60:157–161

[95] Thompson MK, Moroni G, Vaneker T, Fadel G, Campbell RI, Gibson I, Bernard A, Schulz J, Graf P, Ahuja B, Martina F (2016) Design for additive manufacturing: trends, opportunities, considerations, and constraints. CIRP Annals 65(2):737–760

[96] Van Netten JJ, Lazzarini PA, Armstrong DG, Bus SA, Fitridge R, Harding K, Kinnear E, Malone M, Menz HB, Perrin BM, Postema K, Prentice J, Schott KH, Wraight PR (2018) Diabetic foot australia guideline on footwear for people with diabetes. J Foot Ankle Res 11(1):1–14

[97] Vigliotti A, Pasini D (2013) Mechanical properties of hierarchical lattices. Mech 62:32–43

[98] Villanueva CH, Maute K (2017) CutFEM topology optimization of 3D laminar incompressible flow problems. Comput Methods Appl Mech Engrg 320:444–473

[99] Wächter A (2002) An Interior Point Algorithm for Large-Scale Nonlinear Optimization with Applications in Process Engineering. PhD thesis, Carnegie Mellon University

[100] Wächter A, Biegler LT (2006) On the implementation of an interior-point filter line-search algorithm for large-scale nonlinear programming. Math Program 106(1, Ser. A):25–57

[101] Wang Y, Luo Z, Zhang N, Qin Q (2016) Topological shape optimization of multifunctional tissue engineering scaffolds with level set method. Struct Multidiscip Optim 54(2):333–347

[102] Wang Y, Xu H, Pasini D (2017) Multiscale isogeometric topology optimization for lattice materials. Comput Methods Appl Mech Engrg 316:568–585

[103] Watts S, Arrighi W, Kudo J, Tortorelli DA, White DA (2019) Simple, accurate surrogate models of the elastic response of three-dimensional open truss micro-architectures with applications to multiscale topology design. Struct Multidiscip Optim 60(5):1887–1920

[104] Wu J, Clausen A, Sigmund O (2017) Minimum compliance topology optimization of shell-infill composites for additive manufacturing. Comput Methods Appl Mech Engrg 326:358–375

[105] Xie Y, Steven G (1993) A simple evolutionary procedure for structural optimization. Comput Struct 49:885–896

[106] Xu H, Farag A, Pasini D (2018) Routes to program thermal expansion in three-dimensional lattice metamaterials built from tetrahedral building blocks. J Mech Phys Solids 117:54–87

[107] Yan N (2001) A posteriori error estimators of gradient recovery type for elliptic obstacle problems. Adv Comput Math 15(1-4):333–362

[108] Yoon GH (2013) Acoustic topology optimization of fibrous material with Delany–Bazley empirical material formulation. J Sound Vib 332(5):1172–1187

[109] Yu S, Wang C, Sun C, Chen W (2014) Topology optimization for light-trapping structure in solar cells. Struct Multidiscip Optim 50(3):367–382

[110] Zhu JH, Zhang WH, Xia L (2016) Topology optimization in aircraft and aerospace structures design. Arch Comput Methods Eng 23(4):595–622

[111] Zienkiewicz OC, Zhu JZ (1987) A simple error estimator and adaptive procedure for practical engineering analysis. Int J Numer Meth Engng 24:337–357

MOX Technical Reports, last issues

Dipartimento di Matematica
Politecnico di Milano, Via Bonardi 9 - 20133 Milano (Italy)

26/2021 Vigano, L.; Sollini, M.; Ieva, F.; Fiz, F.; Torzilli, G.
Chemotherapy-Associated Liver Injuries: Unmet Needs and New Insights for Surgical Oncologists

27/2021 Scimone, R.; Menafoglio, A.; Sangalli, L.M.; Secchi, P.
A look at the spatio-temporal mortality patterns in Italy during the COVID-19 pandemic through the lens of mortality densities

25/2021 Tenderini, R.; Pagani, S.; Quarteroni, A.; Deparis S.
PDE-aware deep learning for inverse problems in cardiac electrophysiology

24/2021 Regazzoni, F.; Chapelle, D.; Moireau, P.
Combining Data Assimilation and Machine Learning to build data-driven models for unknown long time dynamics - Applications in cardiovascular modeling

23/2021 Scimone, R.; Taormina, T.; Colosimo, B. M.; Grasso, M.; Menafoglio, A.; Secchi, P.
Statistical modeling and monitoring of geometrical deviations in complex shapes with application to Additive Manufacturing

22/2021 Domanin, M.; Bennati, L.; Vergara, C.; Bissacco, D.; Malloggi, C.; Silani, V.; Parati, G.; Trima
Fluid structure interaction analysis to stratify the behavior of different atheromatous carotid plaques

20/2021 Pasquale, A.; Ammar, A.; Falcó, A.; Perotto, S.; Cueto, E.; Duval, J.-L.; Chinesta, F.
A separated representation involving multiple time scales within the Proper Generalized Decomposition framework

21/2021 Torti, A.; Galvani, M.; Menafoglio, A.; Secchi, P.; Vantini S.
A General Bi-clustering Algorithm for Hilbert Data: Analysis of the Lombardy Railway Service

18/2021 Gigante, G.; Vergara, C.
On the choice of interface parameters in Robin-Robin loosely coupled schemes for fluid-structure interaction

16/2021 Salvador, M.; Dede', L.; Manzoni, A.
Non intrusive reduced order modeling of parametrized PDEs by kernel POD and neural networks